Int J Fract (2022) 235:3–46
https://doi.org/10.1007/s10704-022-00641-3

REVIEW PAPER

Fatigue behaviour of laser powder bed fusion (L-PBF) Ti–6Al–4V, Al–Si–Mg and stainless steels: a brief overview

L. Afroz · R. Das · M. Qian · M. Easton · M. Brandt

Received: 19 October 2021 / Accepted: 25 April 2022 / Published online: 23 June 2022

Abstract Fatigue and crack growth characteristics are essential cyclic properties of additively manufactured (AM) components for load-bearing applications, which are less reported in the literature than static properties. The fatigue behaviour of AM components is more complicated than those produced by conventional fabrication techniques (casting and forging) because of the multiplicity of different influencing factors like defect distribution, inhomogeneity of the microstructure and consequent anisotropy. Therefore, it is crucial to understand fatigue performance under different loading conditions to enhance AM application in aerospace, automotive, and other industries. The present work summarises the published literature for fatigue properties of popular metals (Ti–6Al–4V, Al–Si–Mg and stainless steels) produced by the laser powder-bed-fusion (L-PBF) process. Moreover, process parameters, post-processing treatments and microstructures of these alloys are discussed to evaluate the current state-of-the-art of fatigue and crack growth properties of L-PBF metals. The static properties of these alloys are also included to incorporate only those cases for which fatigue behaviour are discussed later in this review to make a correlation between the static and fatigue properties for these alloys. The effects of build orientation, microstructure, heat treatment, surface roughness and defects on fatigue strength and fatigue crack growth threshold are observed and critically analysed based on available literature. This study also highlights the common and contrary findings in the literature associated with various influential factors to comprehensively understand the cyclic loading behaviour of L-PBF produced metal alloys.

Keywords Additive manufacturing (AM) · Laser powder bed fusion (L-PBF) · Fatigue · Fracture · Fatigue crack growth (FCG)

L. Afroz (✉) · R. Das · M. Qian · M. Easton · M. Brandt
Centre for Additive Manufacturing and School of Engineering, RMIT University, Melbourne, VIC 3001, Australia
e-mail: s3731913@student.rmit.edu.au

1 Introduction

Additive manufacturing (AM) is a new and emerging technique that has the potential to produce complex and customised high strength products directly from three-dimensional CAD models. AM is primarily a layer by layer process, which the ASTM has defined as "*a process of joining materials to make objects from 3D model data, usually layer upon layer, as opposed to subtract manufacturing methodologies. Synonyms: additive fabrication, additive processes, additive techniques, additive layer manufacturing, and freedom fabrication*" (Alcisto et al. 2011).

This technology was introduced in the early 1980s in Japan by Kodama (Kodama 1981), who invented the 3D polymerisation process, which is known today as stereolithography. Almost ten years later, E. Sachs et al. (Sachs et al. 1990) successfully printed a 3D building with all its attributes using their novel process. Since then, machines have been improved continuously and employed to develop products of enhanced functionality and often great complexity.

Today an increasing number of manufacturing companies use AM because it can dramatically shorten fabrication time and cost due to the elimination of production and assembly steps and also reduce the material waste and environmental impact compared to conventional processing. Although AM metals have benefits over casting, the AM technologies are still associated with the inevitable presence of processing defects such as pores, lack of fusion pores, cracks and impurities, and can lead to a build-up of residual stresses (Li et al. 2018). Several other factors, such as raw material characteristics, chemical composition, powder density distribution, process parameters, and post-processing, affect the resultant part properties (Mahmoudi et al. 2017). Furthermore, additive manufacturing (Appleyard 2015) transforms powder materials into solid geometries (components) at high solidification rates, which affects the microstructure of the deposited material and hence the mechanical properties. Although extensive research effort has been directed to characterise the AM parameters, the uncertainty of the load-bearing properties of 3D printed structures is still a challenge, yet to be fully addressed for different AM processes (Frazier 2014; Sterling et al. 2016).

Various AM techniques are available depending upon the material to be fabricated and the mechanism of layer formations. However, this review only focuses on the metal alloys produced by Laser Powder Bed Fusion (L-PBF) (Frazier 2014), often also called Selective Laser Melting process (SLM) (*SLM Solutions GmbH*). L-PBF produces complex-shaped components with several structural alloys to meet the requirements in different fields, such as aerospace, automotive, and biomedical applications (Herzog et al. 2016).

With the advancement of AM techniques, many researchers have paid attention to understanding the effects of different factors on the mechanical and microstructural properties of AM materials. The majority of the work has focused on the static mechanical (tensile/compression) properties of the popular AM alloy, Ti–6Al–4V alloy (Daniewicz and Shamsaei 2017; de Formanoir et al. 2016; Gong et al. 2015; Lewandowski and Seifi 2016; Qian et al. 2016; Rafi et al. 2013a; Simonelli et al. 2014). Only a few studies have concerned with other AM alloys, such as AlSi10Mg (Brandl et al. 2012; Read et al. 2015; Siddique et al. 2017) and stainless steel (Rafi et al. 2013b; Spierings et al. 2011). In general, most AM materials and processes outperform their conventional counterparts in terms of static strength (Buchbinder et al. 2011; Herzog et al. 2016). This is because of the finer microstructure from L-PBF generated by the rapid melting and cooling process (Brandl et al. 2012). However, porosity and defects are often unavoidable features of bulk AM fabricated parts. The presence of pores does not reduce the stiffness or the yield strength (Read et al. 2015). However, it can act as a crack initiator under cyclic loading, thus reduce the fatigue strength by about 40–50% (Gong et al. 2015; Leuders et al. 2013). Furthermore, fatigue failure of AM metals is more complicated than conventional fabrication because of the involvement of different influencing factors, for example, the inhomogeneous microstructure and varying pore size and orientation with the change in process parameters (Cao et al. 2018).

The presence of various AM defects and microstructural inhomogeneities is affected by the processing parameters. Furthermore, the presence of residual stress and surface roughness may cause degradation in material properties. Therefore, this review aims to interpret the change in mechanical properties for different AM parameters and post-processing treatments. The static failure mechanisms are always a fundamental matter of interest, and therefore, has been reviewed (Agius et al. 2018; Bai et al. 2017; Herderick 2011; Trevisan et al. 2017; Zhang et al. 2017) by a number of researchers for AM alloys. Therefore, this work will focus more on fatigue and fatigue fracture behaviours of AM produced alloys, particularly for the L-PBF process.

In recent years, the fatigue and fatigue failure behaviour of AM alloys have become a focal point (Cao et al. 2018; Gorsse et al. 2017; Lewandowski and Seifi 2016; Yadollahi and Shamsaei 2017). To date, there have been some reports on the fatigue properties of Ti–6Al–4V (Agius et al. 2018; Frazier 2014; Gorsse et al. 2017; Li et al. 2018; Saboori et al. 2017; Tong

et al. 2017; Yadollahi and Shamsaei 2017), but fewer on Al–Si–Mg (Aboulkhair et al. 2019; Trevisan et al. 2017) and steels (Afkhami et al. 2019). In a review, Herzog et al. (Herzog et al. 2016) have reported the overall static and fatigue strength of AM materials while Cao et al. (Cao et al. 2018) and Tong et al. (Tong et al. 2017) summarized the quantitative understanding of the fatigue behaviour in particular for Ti–6Al–4V alloy. Yadollahi and Shamsaei (2017) provided an overview of the fatigue characteristics of AM materials. Other articles (Aboulkhair et al. 2019; Trevisan et al. 2017; D. Zhang et al. 2018a, b, c) have studied the state-of-the-art Al alloys produced via L-PBF processes, considering the effect of various factors on the microstructure and mechanical behaviour. The limited data available for fatigue and fracture toughness of AM produced metals leads to uncertainty in the durability assessment of AM parts. Therefore, it is imperative to have a thorough understanding of the fatigue behaviour of additively manufactured alloys to improve the reliability of AM fabricated parts.

In this context, this review aims to focus on the currently available fatigue, and fatigue crack growth data of L-PBF produced common alloys, namely titanium (Ti–6Al–4V), aluminium (Al–Si–Mg) and stainless steels (316L, 17-PH), to draw up a state-of-the-art portrait of the present literature. This review also intends to analyse the effects of heat treatment, microstructure and anisotropy on the overall mechanical fatigue behaviour to identify the current knowledge limitations. An organizational structure of this study is included in Fig. 1.

2 Additive manufacturing (AM)

The basic principle of an AM system is to generate a 3D computer CAD model of a component and then print it using a layer by layer process by melting powder or wire feedstock. There are many AM technologies available commercially which have their advantages and disadvantages associated with the intended application. In this section, AM technologies, process parameters and microstructure will be discussed to correlate the effect of these factors on the fatigue of various metal alloys (Edgar and Tint 2015; Frazier 2014; Herzog et al. 2016).

2.1 Types of additive manufacturing

Additive manufacturing processes can be categorised in several ways depending upon the material to be fabricated and the mechanism in which the layers are developed. Frazier (Frazier 2014) has divided the AM system into three board categories as (i) powder bed systems, (ii) powder feed systems and, (iii) wire feed systems.

Powder bed fusion (PBF) system can fabricate complex parts with a higher degree of freedom by directly melting powder metal (Kruth et al. 2005) and has gained popularity in producing light-weight parts (Maskery et al. 2015b) and functionally graded material (Maskery et al. 2016a). PBF has three steps: uniform deposition of powder on the bedplate from a hopper or a powder reservoir to create a thin layer, the exposure of an energy source onto the bed to locally melt the powder, and finally lowering the build plate to rake another layer of powder when the first layer is completely solidified. These steps continue until the completion of designed metal parts (Van der Schueren and Kruth 1995). Based on the energy source used, the powder bed fusion system is further be classified into two categories: Laser powder bed fusion (L-PBF) and Electron beam powder bed fusion (E-PBF).

Both L-PBF (*EOS Electro Optical Systems GmbH,*; *Trumpf GmbH*) and E-PBF have the same basic operational principles; however, E-PBF uses an electron beam (Murr et al. 2010, 2012a) as the energy source instead of a laser beam (*Concept Laser GmbH*) as used in L-PBF. L-PBF requires an inert gas atmosphere to ensure that the residual oxygen content is no more than 0.1% (Attar et al. 2014). Nitrogen or argon is fed into the chamber to protect the metal powder from oxidation and to carry away any by-product spatter from the main part (Ferrar et al. 2012). On the contrary, for the E-PBF process, the operational environment is a vacuum ($< 10^{-4}$ Pa) to avoid any electron charging as well as to enhance the heat conduction process (Murr et al. 2012a).

In contrast to PBF system, powder feed systems or laser direct energy deposition (L-DED) systems use nozzles to feed the powder into the work surface. L-DED enables large volume scale production at a higher built rate. Two different systems of L-DED are possible, one in which the work part is stationary while the deposition head moves for each layer of the build.

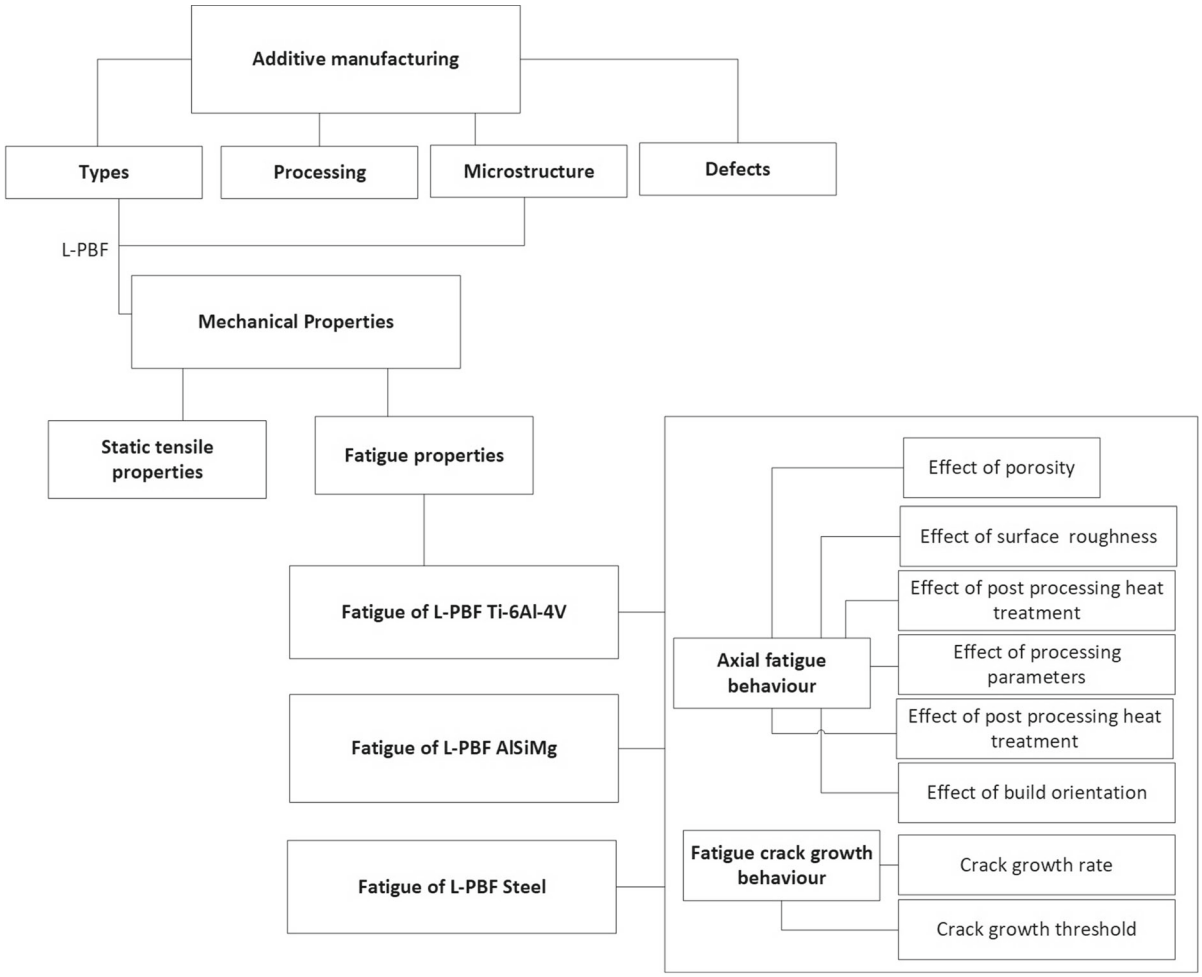

Fig. 1 Organizational structure of the review

In the other type, the deposition head remains stationary with a moving workpiece (Frazier 2014).

Wire feed system, also known as Laser beam free-form fabrication, is a modified version of the powder feed system in which the wire is used as a feedstock instead of powder (Frazier 2014). The energy source for this process can be an electron beam, laser beam or plasma arc. The wire feed process is suited to a large build volume; however, it requires more rigorous and careful post-processing than PBF or DED.

Among all these AM technologies, L-PBF is popular with the automotive and aerospace industry; therefore, it will focus on this review.

2.2 AM process parameters

Both powder properties and machine parameters influence the microstructure and mechanical properties of AM parts (Das 2003; Louvis et al. 2011; Sercombe and Li 2016). In metal powder-based processes, the powder morphology, particle size, chemical composition and thermal conductivity are crucial to the success of the AM process. Moreover, to achieve high-density bulk material, good flowability of particles is required, which maintains homogeneity while spreading over the bed. Spherical powder leads to better packing density than irregular powder particles, as the flow time is reduced (Dawes et al. 2015; Olakanmi 2013).

The machine parameters such as laser power, scan speed, hatch spacing, and layer thickness significantly influence the final AM part. These parameters contribute directly to the part density (Gu 2015), phase stability, anisotropy and microstructure (Ahn et al. 2002; Shamsaei et al. 2015). By varying process parameters, an optimal energy range can be found relative to the machines and alloys to be printed (Leary et al. 2018; Meier and Haberland 2008; Yadroitsev et al. 2007).

The laser scanning strategy (scan vector length and rotation) is a geometrical pattern that the beam follows during the powder melting process. The commonly adopted strategies are single melt (with different scan rotation) and chessboard, as illustrated in Fig. 2. Scanning strategy may affect the residual stress generation, porosity formation, anisotropy behaviour, and mechanical properties (Aboulkhair et al. 2016b; Ali et al. 2018; Carter et al. 2014; Spierings et al. 2011).

Build orientation of parts in the build plate (Fig. 3) affects the microstructural direction, defects and consequently, mechanical properties (Kimura and Nakamoto 2016; Read et al. 2015; Yadollahi et al. 2017).

Build platform heating is another crucial parameter for the L-PBF process. Pre-heating of the platform reduces the thermal gradient between the layers, thus providing a relatively low cooling rate. Therefore, elongated dendrites can be observed for pre-heated samples as it allows more time in the solidification process (Siddique et al. 2017). Pre-heating also reduces residual stress and cracking (Kempen et al. 2013).

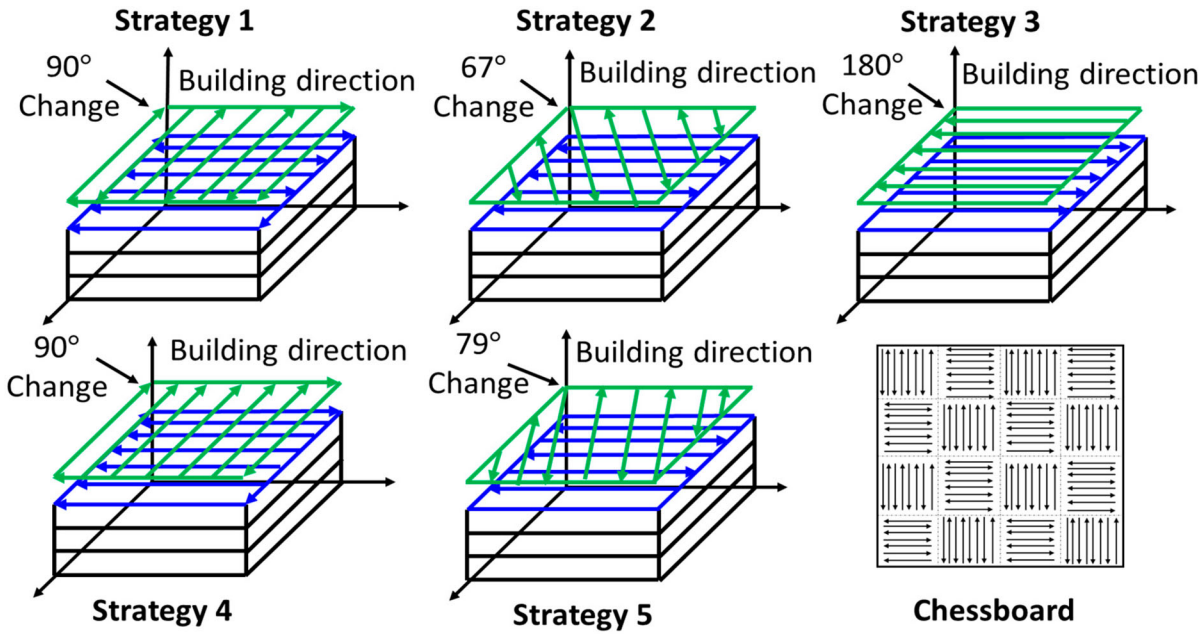

Fig. 2 Scanning strategies in AM process (Agius et al. 2018)

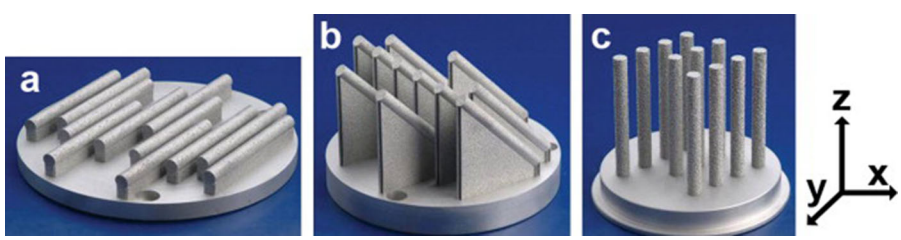

Fig. 3 Build orientations: **a** horizontal (0°), **b** diagonal (45°), and **c** vertical (90°) (Brandl et al. 2012)

The machine parameters used to produce the fatigue samples discussed in this study are listed in Table 1.

2.3 Microstructure characteristics

In AM, the material undergoes a complex thermal cycle which includes a large number of rapid melting and subsequent solidification processes. The microstructure of AM processed material is, therefore, a result of this thermal process, which is more complex to analyse in comparison with cast material (Gong et al. 2014a, b). Moreover, different AM methods use different operating parameters—laser energy, layer thickness, energy density and preheating temperature, which also influence the microstructure. The evolution and effect of microstructure on the mechanical properties are discussed in the following sections for AM produced Ti, Al and Steels.

2.3.1 Microstructure of L-PBF Ti–6Al–4V

The typical microstructure for wrought Ti–6Al–4V has a globular α phase with α + β matrix, as shown in Fig. 4a. However, AM microstructure looks quite different and is affected by the process parameters, post-processing heat treatment and types of AM methods (Kasperovich and Hausmann 2015; Murr et al. 2012b; Qiu et al. 2013). In the case of the L-PBF processing, acicular α' martensitic (Fig. 4b) and columnar prior β grain boundaries are commonly found (Chen et al. 2017; Qiu et al. 2013; Simonelli et al. 2014; Xu et al. 2015). Columnar β grains are parallel to the build direction, as a result of the high thermal gradient and high cooling rate in the AM process. EBSD maps in Fig. 4d and e show α' phase and reconstructed β phase, respectively, for L-PBF Ti–6Al–4V, where z indicates the build direction. The grain size of this martensitic α' depends on the thermal cycle and reheating process. With a change in processing parameters to control the thermal conditions, the microstructure can be either martensitic α' or lamellar α/β (Xu et al. 2015).

The transformation of martensitic to lamellar microstructure can be achieved by either post-heat treatments or preheating the build plate (Ali et al. 2017; Greitemeier et al. 2017; Kasperovich and Hausmann 2015). A metastable martensitic phase of Ti associated with rapid cooling in the L-PBF process reduces the ductility of the material (Dallago et al. 2018), however, provides better fatigue strength. On the other hand, higher fracture toughness and a reduction in fatigue growth rate can be achieved by a lamellar α + β microstructure (Lütjering 1998). The lamellar microstructure causes coarsening of grain structure. This may lead to a reduction in fatigue performance and yield strength. However, Kasperovich and Hausmann (2015) have shown that lamellar microstructure obtained at a high temperature (around 900 °C) can regain the typical martensitic Ti properties (high tensile and fatigue strength), similar to globular microstructure but with elongated columnar grain as shown in Fig. 4c.

The microstructure formation in Ti-alloys is also controlled by process parameters (Xu et al. 2015; Zhai et al. 2015) and build orientation (Agius et al. 2017). Agius et al. (2017) found a coarser α′ martensitic structure for horizontal build (0°) samples, while diagonally (45°) and vertically (90°) orientated samples showed ultrafine α′ martensitic microstructure. The position of samples on the build plate along with the variation of gas flow (hence thermal conditions) is the reason for the formation of ultrafine α′ martensitic microstructure. Both the static and cyclic strengths are found to be higher for diagonally orientated samples attributed to the formation of fine microstructure and their uniform distribution in coarse α′ martensite. This supports the finding of Wu et al. (Wu et al. 2013), who revealed that higher crack initiation resistance and improved fatigue strength is associated with finer grain sizes. However, the fine microstructure also allows rapid crack propagation, thus increasing the crack growth rates. This means a longer crack growth duration will be enabled by a course lamellar microstructure for Ti-alloy. This is supported by a work of Agius et al. (2018) on Ti-alloys, whereby it has been suggested that a fine lamellar microstructure (with α lamellae width less than 1 μm) delays crack initiation of pores under cyclic loading, whereas course lamellar reduces crack growth rates.

2.3.2 Microstructure of L-PBF Al–Si–Mg

Traditionally cast AlSi10Mg alloy forms a homogenous mixture of primary α-Al and eutectic Al-Si structure with coarse Si particles, as shown in Fig. 5a. In contrast, in L-PBF, cellular dendrites of α-Al with eutectic Si network at the boundaries is found

Table 1 L-PBF parameters used to manufacture Ti, Al and steel fatigue coupons

Alloy	AM machine	Lase power (W)	Scan speed (mm/s)	Hatch spacing (μm)	Layer thickness (μm)	Build orientation	Base plate temperature (°C)	Scanning strategy	Particle size (μm)	References
Ti–6Al–4V	EOS M270	200	1250	170	100	–	30	180°	38	Rafi et al. (2013b)
	EOS M270	200	–	–	30	Z, XZ	–	–	20–63	Wycisk et al. (2015)
	EOS M270	120	960 540 400 1260 1500	100	30	Z	–	–	30	Gong et al. (2015)
	Concept Laser M2	200	1250	–	40	Z	–	–	35	Kasperovich and Hausmann (2015)
	SLM 250HL	400	–	–	30	Z	100	–		Leuders et al. (2013)
	SLM 250HL	375	686–1029	120	60	Z	200	Chessboard	25–45	Xu et al. (2015)
	MTT 250 machine	200	200	180	50	–	–	67°	30	Edwards and Ramulu (2014)
	EOS M280	370	–	–	60	–	35	0° and 90°	–	Greitemeier et al. (2017)
	3D systems ProX 300 printer	–	–	–	–	–	–	–	9	Benedetti et al. (2018)
	Renishaw AM250	157	225	100	50	XY, Z	–	67°	–	Simonelli et al. (2014)
AlSi10Mg	EOS M280	370	1300	160 190 220	30	XY Z	NR	67°	–	Tang and Pistorius (2017)
	EOSINT M280	400	1000	200	30	Z	350	Back and forth (90°)	–	Uzan et al. (2017)
	SLM 280HL	500–700	1200–1700	–	60	XY, Z	–	–	45	Awd et al. (2017)
AlSi12Mg	SLM 250HL	350	930	190	50	XY	0 200	79°	–	Siddique et al. (2017)
	SLM 250HL	350	921	190	50	XY, Z	200	67°	–	Zhao et al. (2018)
	Trumpf TumaForm LF 130	250	500	150	50	XY Z	30 300	–	–	Brandl et al. (2012)
	SLM 280	100	930	100	50	XY Z	200	–	–	Mower and Long (2016)
	Reinshaw AM 250	200	570	80	25		180	Chessboard	–	Aboulkhair et al. (2016a)
	EOS M400	1000	–	90	60	XY Z	200	–	–	Romano et al. (2018)
	Concept Laser M2 cusing system	175	1025	97.5	30	XY Z	–	90°	–	Larrosa et al. (2018)

Table 1 continued

Alloy	AM machine	Lase power (W)	Scan speed (mm/s)	Hatch spacing (μm)	Layer thickness (μm)	Build orientation	Base plate temperature (°C)	Scanning strategy	Particle size (μm)	References
	SLM 250HL	–	1455	110	50	XY, Z	–	73° Single Melt Checkerboard	20–120	Suryawanshi et al. (2016)
Al360	–	–	–	–	Cast	–	165	315		ASTM B85-03, Standard Specification for Aluminum-Alloy Die Castings
PH1	EOS M270	200	800	195	100	–	40	180°	43	Rafi et al. (2013b)
15-5PH	EOS M270	195	800	100	20	–	–	–	–	Wegener et al. (2013)
17-PH	SLM (PROX^{TM}100)	48	300	50	30	XY, Z	–	–	22	Yadollahi et al. (2017)
18Ni (300) MS	Concept Laser M2	180	600	105	30	XY, Z	–	30° and 100°	20–50	Suryawanshi et al. (2017b)
18Ni (300) MS	Concept Laser M2	200	–	–	30	XY, Z	–	Chessboard	43	Hermann Becker and Dimitrov (2016)
316L stainless steel	SLM 250HL	400	–	–	30	XY	100	–	40	Riemer et al. (2014)
	Concept Laser	90	100	150	30	XY, Z	–	90°, Chessboard	–	Suryawanshi et al. (2017a)
	Concept Laser M1	103	425	130	30	–	–	Chessboard	–	Wegener et al. (2013)
	SLM 250HL	275	760	120	50	–	–	–	20–63	Uhlmann et al. (2017)

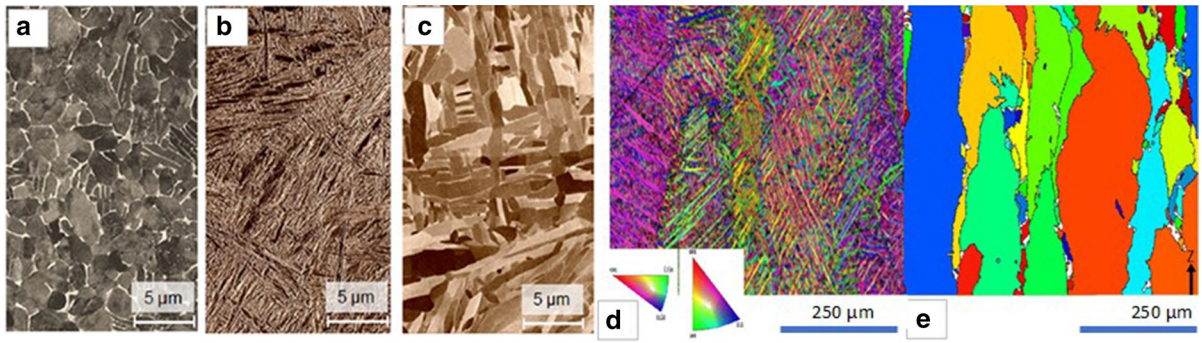

Fig. 4 Microstructure of Ti–6Al–4V: **a** globular α + β structure of wrought processing, **b** L-PBF acicular α′ (fully martensitic) structure, **c** L-PBF lamellar (α + β) structure (Kasperovich and Hausmann 2015), EBSD map of Ti–6Al–4V **d** α′ phase, **e** reconstructed β phase (Neikter et al. 2019)

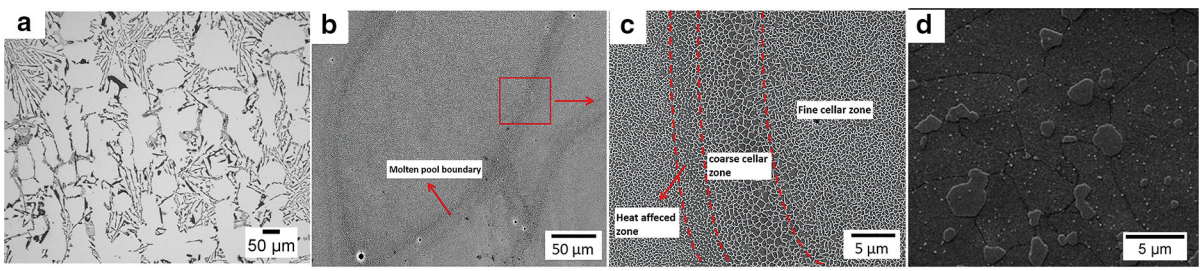

Fig. 5 Microstructure of Al-alloys: **a** cast AlSi10Mg alloy (Takata et al. 2017), **b** L-PBF AlSi10Mg alloy at low magnification, **c** high magnification image showing HAZ (horizontal cross-section) (Kong et al. 2019), **d** spheroids of Si particle after T6 in AlSi10Mg (no visible laser tracks) (Fousova et al. 2018)

(Trevisan et al. 2017). The fast cooling rates in L-PBF enhances the solubility of Si in Al, and the excess Si accumulates along the cellular grain boundaries yielding a fine microstructure (Prashanth et al. 2014a). Figure 5b shows the visible laser tracks in L-PBF Al-12Si alloy. The microstructure of L-PBF Al-alloy is not uniform for the whole cross-section, preferably with a transition from fine to coarse cellular dendrites along the heat-affected zone, as shown in Fig. 5c. The fine cellular eutectic region is found in the as-built samples due to fast cooling while boundaries of the melt pools have coarse microstructure for slow cooling rate (Awd et al. 2017; Liu et al. 2019). The average sizes of Al dendrites and Si particles are around 500–1000 nm and 200 nm (Prashanth et al. 2014a) respectively, for L-PBF fabrication which is very fine compare to conventional casting. The fine microstructure of the as-built Al-alloy due to rapid cooling leads to high hardness, yield and tensile strength.

Solution heat treatment defuses Si into spheroid type particles (Fig. 5d); removing the heat affected zone and makes the structure more homogenous (Brandl et al. 2012; Uzan et al. 2017). Heat treatment reduces the anisotropy in the microstructure. The spherodization of eutectic phase is also observed for specimens built with base plate heating. Base plate heating results in a higher average width of dendrites compared to those built without base plate heating (Siddique et al. 2015), which in turn increases the fatigue strength but causes a decrease in hardness and tensile strength (Siddique et al. 2017). The crack growth propagation rate is also less for base plate heated specimens due to elongated dendrites. Heat conduction is higher in the build direction; therefore, more elongated grains are observed along with the build direction (Kimura and Nakamoto 2016; Tan et al. 2015).

2.3.3 Microstructure of L-PBF steels

The most common types of steel that are 3D printed are 316L and 17-PH steel. Unlike conventional processes, a finer and elongated microstructure is found in AM steel parts due to the high cooling rate

(Jägle et al. 2014; Kempen et al. 2014). Melt pool boundaries are easily visible (Fig. 6a) for almost all AM steel parts (Gu et al. 2013; Mower and Long 2016; Sun et al. 2015; Zheng et al. 2008) which may contain non-metallic elements like C, O, and Si (Shifeng et al. 2014). Coarsening of the microstructure happens in the part which is away from the build plate, owing to a reduction of the temperature gradient.

AM 316L steel forms equiaxed grains at the melt pool with dendritic columnar structure around the boundaries, as shown in Fig. 6b. EBSD map, as in Fig. 6c, shows the crystal orientation of 316L in the build direction. The white arrows indicate orientation gradient in the same grain in case of L-PBF 316L. Like 316L, L-PBF 17-PH steel has a microstructure with visible melt pool and large (columnar) grains along the melt pool boundaries, as in Fig. 7a. However, heat treatment makes the laser track invisible (Fig. 7b). The microstructure for 316L steel can be 100% austenitic for an as-built condition. On the other hand, typical martensitic steels such as 17-PH can have a certain amount of retained austenite between the martensitic phase (Facchini et al. 2010; LeBrun et al. 2015).

The above fact demonstrates that microstructure is an essential feature of AM processed metals, highly affected by processing and post-processing parameters. This change influences both the static and cyclic mechanical behaviour of the parts fabricated by AM, which will be discussed more in Sects. 3 and 4.

2.3.4 AM defects and formation

One of the fundamental challenges of AM is the generation of various inhomogeneities and defects during the fabrication process (Gu and Shen 2009; Lee and Farson 2016; Li et al. 2012; Sola and Nouri 2019; Yang et al. 2018; Zhang 2013; Zhao et al. 2009). Almost all AM processes produce internal defects that may be acceptable but within a tolerable limit based on the product's mechanical performance requirement.

The most commonly observed AM defect is bulk porosity (Banerjee et al. 2005; Frazier 2014; Sola and Nouri 2019). The formation of AM porosity is strongly affected by variations in the process parameters (Buchbinder et al. 2011), and can occur from a number of sources (Ng et al. 2009), as shown in Fig. 8. Both powder properties (Liu et al. 2011) and machine parameters (Gu and Shen 2009; Khairallah et al. 2016; Thijs et al. 2013) influence the formation of pores, their size and density. Powder properties, e.g., size, density and composition, are other fundamental factors controlling the defects of AM metal (Ahsan et al. 2011; Liu et al. 2011; Zhang et al. 2017). Contaminations of moisture, gases and organics in the powder hinders the densification process and leads to pore formations (Weingarten et al. 2015).

Metallurgical pores also referred to as gas pores, (Weingarten et al. 2015) are usually spherical in shape and less than 100 μm in size (Yang et al. 2018; Zhang et al. 2017). Gas pores form due to the presence of moisture on the surface of the powder feedstock leading to H_2 absorption in the melt (Gong et al. 2014a, b; Weingarten et al. 2015). The irregular shaped pores found in AM parts can be identified as key-hole or Lack of fusion pores (LOF), formation of which is more controlled by energy density input (Shrestha et al. 2019). A very high energy density (exceeding boiling point) within the melt pool leads to

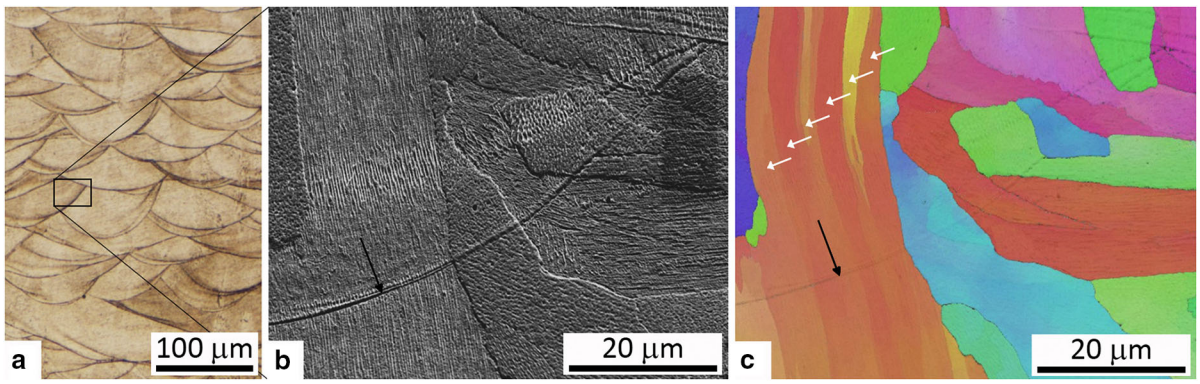

Fig. 6 L-PBF fabricated 316L steel **a** optical microscope image, **b** secondary electron image showing cell structure, **c** EBSD map showing grain orientation along the build direction (Godec et al. 2020)

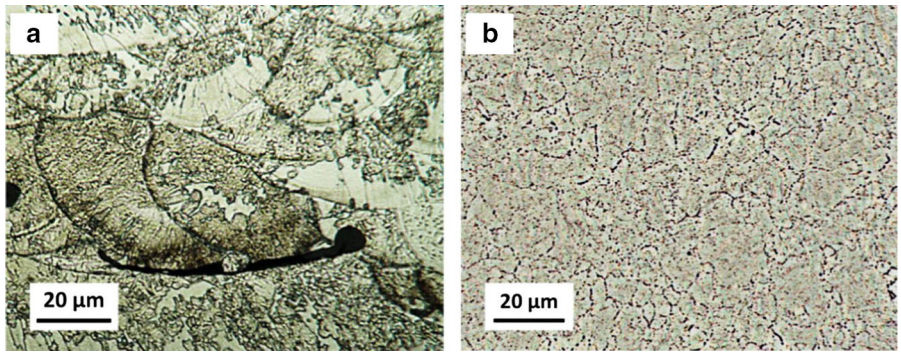

Fig. 7 L-PBF 17-PH steel **a** as-fabricated, **b** after heat-treatment (Mahmoudi et al. 2017)

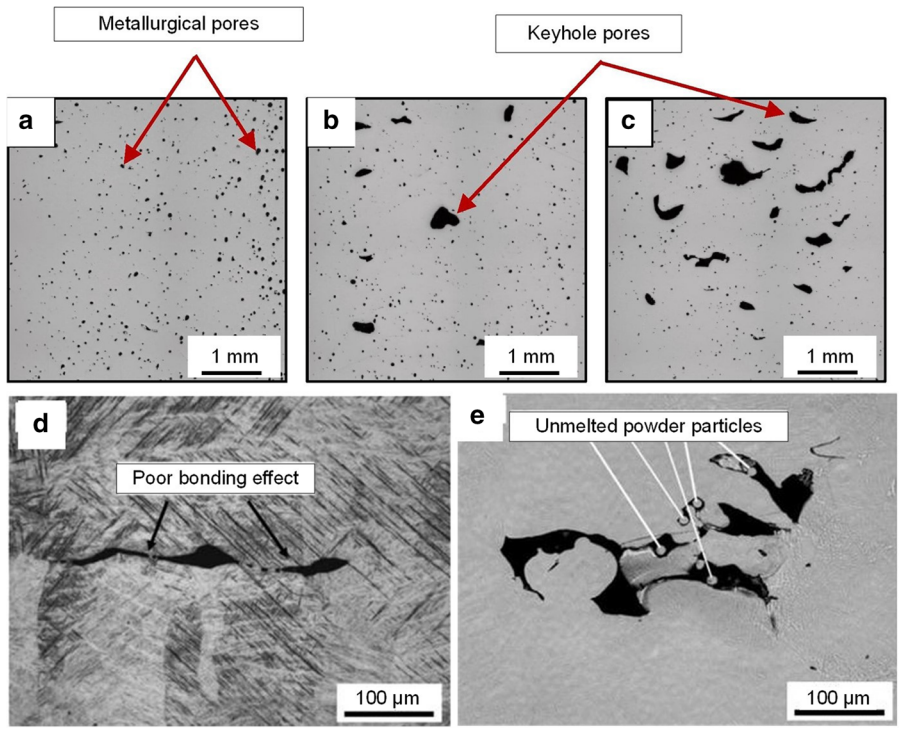

Fig. 8 **a** Entrained gas porosity in L-PBF AlSi10Mg, **b** Lower key-hole pores at slow scan speed and **c** higher number of keyhole pores at fast scan speed in L-PBF AlSi10Mg (Aboulkhair et al. 2019), and **d** LOF due to poor bonding, **e** LOF pores with un-melted powders inside (L-PBF Ti–6Al–4V) (Liu et al. 2014)

material evaporation. The evaporation of material generates evaporation pressure that forms deep depression on the part known as key-hole pores (King et al. 2014). A fast scan speed associated with low heat input forms more irregular and elongated pores (Kang et al. 2018; Qiu et al. 2013; Vilaro et al. 2011) in AM parts due to insufficient heating of the previous layer, known as LOF pores (Carter et al. 2015; Vilaro et al. 2011). However, high energy input is claimed to reduce overall porosity density in many studies (Hann et al. 2011; Rai et al. 2007; Wu et al. 2014).

Two types of LOF pores is found in AM parts: inadequate re-melting between the layers during the solidification process and incomplete (partial) melting of powders, as shown in Fig. 8. For the latter case, LOF defects contain un-melted powder particles. LOF pores are mostly found near the melt pool boundaries or in-between scanning layers. In addition to energy input, an adequate overlapping of laser tracks between layers and preheating of the bedplate also reduce the density of LOF porosity (Siddique et al. 2017) as well as hydrogen porosity formation (Weingarten et al. 2015), by improving the wettability of the melt pool.

Preheating of the base plate also reduces the residual stress within the part, along with susceptibility to crack formation by reducing the thermal gradient (Carter et al. 2014; Kempen et al. 2014). Interlayer defects may also form due to the presence of pre-generated defects on the previous layer, which reduces the flowability of the molten metal and thus leads to weak bonding between the layers. Besides, insufficient inert gas flow during the L-PBF process may cause trapping of the by-products, which in turns increases the lack of fusion defects. Moreover, inert gas itself can be a reason for the formation of gas pores if non-uniform recoil pressure occurs within the melt pool surface (Gu and Shen 2009).

The scanning strategy also controls the solidification process and affects the defect formation and location. The unidirectional or zigzag scanning process produces more LOF pores between the layers (Bauereiß et al. 2014; Maskery et al. 2016b), whilst, chessboard or island scan strategy is the most successful in reducing repetitive defect accumulation in the same location (Read et al. 2015).

Both gas and LOF pores in AM parts can be detrimental for mechanical properties such as fracture toughness and fatigue strength, particularly if pores are found to be highly concentrated in one place or near the surface (Beretta and Romano 2017; Zhao et al. 2018).

Surface roughness is another crucial defect of AM parts, which is detrimental to fatigue performance (Cao et al. 2018; Sterling et al. 2016). Compared to conventional manufacturing, AM causes higher surface roughness in the as-built condition (Fig. 9) due to partially-melted particles adhering to the surface (Anil et al. 2011). The surface defects or features are highly affected by build orientation (Beretta and Romano 2017; Fox et al. 2016), build rate (Frazier 2014) and energy deposition and scanning strategy (Koutiri et al. 2018). An increase in build rate causes reduced surface quality (Meier and Haberland 2008). Moreover, in the L-PBF method, while printing the part in an inclined position, the downward-facing side produces more surface irregularities (Fig. 9c) due to thermal edge effects (Yadollahi and Shamsaei 2017). Laser re-melting has been proposed to decrease surface roughness in steel (Yasa and Kruth 2011).

From the above discussion, it is evident that the process parameters affect defect formation in AM. For example, a reduction in laser power may produce less gas porosity. However, it may lead to the generation of more LOF pores. Therefore, optimization of process parameters based on their interrelationships as well as the future application of the parts may help to reduce defect accumulation and improve mechanical performance.

3 Static properties

The static mechanical properties of AM metal parts are often higher than those made by conventional fabrication (forging, casting, etc.) techniques. This is because of the fine microstructure generated in the AM manufactured alloys. Many research efforts have been directed to understand and compare the static mechanical properties that include tensile, compressive, hardness properties of AM parts (Aboulkhair et al. 2019; Agius et al. 2018; Kong et al. 2019; Lewandowski and Seifi 2016; Liu and Shin 2019; Prashanth et al. 2014a; Trevisan et al. 2017). Table 2 and Fig. 10 present an extract of the static data to show the comparison of tensile and yield strengths of AM

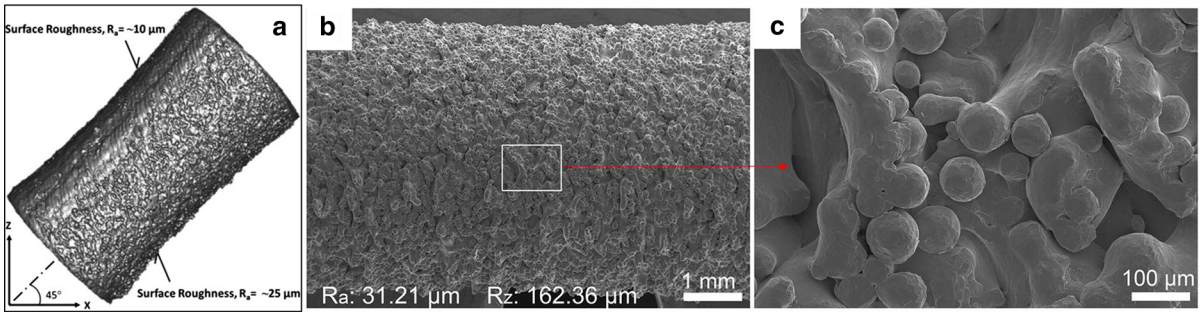

Fig. 9 Surface roughness in **a** as-built Ti–6Al–4V, **b** high magnification section of image a (Sun et al. 2020), and **c** Inconel 718 fabricated at 45° orientation (Yadollahi and Shamsaei 2017)

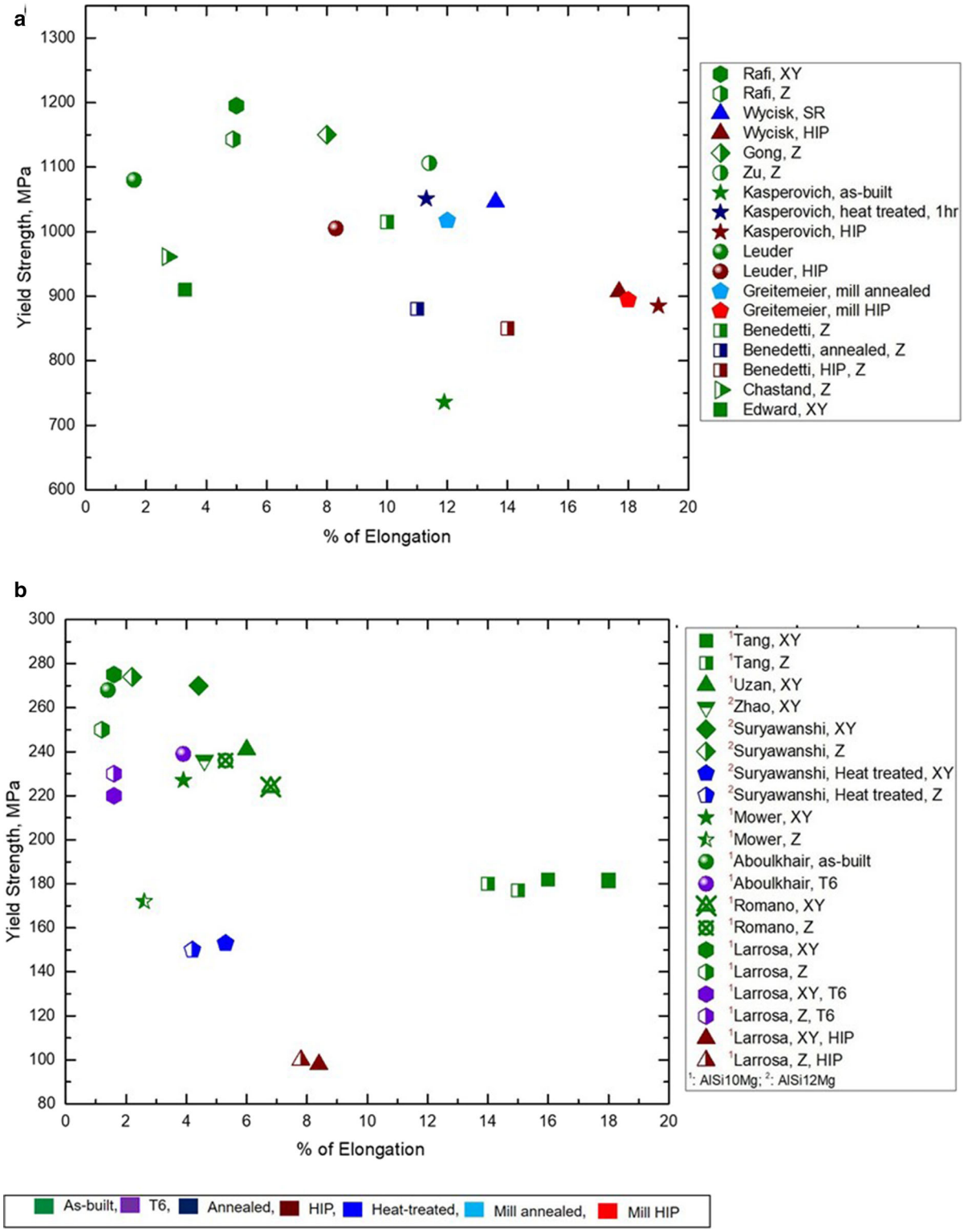
a
Yield Strength, MPa
% of Elongation
Rafi, XY
Rafi, Z
Wycisk, SR
Wycisk, HIP
Gong, Z
Zu, Z
Kasperovich, as-built
Kasperovich, heat treated, 1hr
Kasperovich, HIP
Leuder
Leuder, HIP
Greitemeier, mill annealed
Greitemeier, mill HIP
Benedetti, Z
Benedetti, annealed, Z
Benedetti, HIP, Z
Chastand, Z
Edward, XY
b
Yield Strength, MPa
% of Elongation
[1]Tang, XY
[1]Tang, Z
[1]Uzan, XY
[2]Zhao, XY
[2]Suryawanshi, XY
[2]Suryawanshi, Z
[2]Suryawanshi, Heat treated, XY
[2]Suryawanshi, Heat treated, Z
[1]Mower, XY
[1]Mower, Z
[1]Aboulkhair, as-built
[1]Aboulkhair, T6
[1]Romano, XY
[1]Romano, Z
[1]Larrosa, XY
[1]Larrosa, Z
[1]Larrosa, XY, T6
[1]Larrosa, Z, T6
[1]Larrosa, XY, HIP
[1]Larrosa, Z, HIP
[1]: AlSi10Mg; [2]: AlSi12Mg
As-built, T6, Annealed, HIP, Heat-treated, Mill annealed, Mill HIP

◀**Fig. 10** Comparison of yield strength and % of elongation of L-PBF **a** Ti–6Al–4V alloy, **b** Al–Si–Mg alloy under different build orientations and heat-treated conditions (data are from literature and re-plotted Aboulkhair et al. 2016b; Benedetti et al. 2018; Edwards and Ramulu 2014; Greitemeier et al. 2016; Larrosa et al. 2018; Leuders et al. 2013; Mower and Long 2016; Rafi et al. 2013b; Romano et al. 2018; Suryawanshi et al. 2016; Tang and Pistorius 2017; Zhao et al. 2018))

manufactured Titanium, Aluminium and steels. These figures do not include all the available static data in the literature but incorporate those cases for which fatigue behaviour are discussed later in this review to make a correlation between the static and fatigue properties for these alloys.

In general, static strength of AM alloys is higher compared to wrought, cast or mill annealed alloys. This is due to the higher density (> 99.5%) than casting and finer microstructure offered by the AM processes over the conventional fabrication processes (Herzog et al. 2016), although AM alloys show inferior elongation properties. The static properties (tensile strength and elongation) of Ti–6Al–4V and Al-alloy have been plotted in Fig. 10.

Figure 10 shows notable scatter in tensile and elongation values due to the variation in defect formation (Vilaro et al. 2011), microstructure (Aboulkhair et al. 2016b; Xu et al. 2015), and build orientations (Herzog et al. 2016). As-built samples show higher yield strength and lower elongation properties, as indicated by green points in Fig. 10. For Ti-alloy, an increased elongation value with reduced yield strength is observed after different heat treatments. Heat treatment reduces the strength by transforming α' martensite into course lamellar $\alpha + \beta$ microstructure (as mentioned in Sect. 2.3.1. However, after heat treatment, the β phase's inclusion allows two-phase slip transfer (Simonelli et al. 2014), thus increasing the plasticity and elongation value. Al-alloy shows the highest static strength in as-built condition with very inferior elongation property. The high strength in Al-alloy is associated with the rapid solidification process, which allows increased Si solubility into α-Al. On the contrary, heat treatment causes the excess Si particles to precipitate along the hatches overlaps (Suryawanshi et al. 2016), and increases the α-Al size at the same time (Prashanth et al. 2014b), thus reduces strength and increases the ductility. However, heat treatments of Al do not lead to a similar change in yield strength or elongation value among the available literature (Fig. 10). The variation in static properties of Al-alloy can be due to the variation in machine parameters, as mentioned in Table 1.

Build orientation is the other factor that causes variation in static properties of L-PBF alloys. In most cases, the horizontally built samples show higher static strength than vertical or orthogonal samples in as-fabricated conditions. This is due to the microstructure formation and grain orientation (Banerjee and Williams 2013). Yang et al. (2017) showed that grain orientation in vertically built samples promotes dislocation movement and consequently lowers yield strength. The anisotropy in tensile strength is due to the presence of defects since defects cause early failure (Gong et al. 2015). The difference in elongation property is partially due to LOF pores in between layers, which causes the vertical samples to fail early by expanding the pores along the loading direction (Vilaro et al. 2011). The influence of machine parameters and microstructure on the defect formation and mechanical properties has been described in Sects. 2.3, and 2.4.

4 Fatigue properties

Much recent work has focused on the static mechanical properties of the different AM alloys. However, the durability of AM products in various load-bearing engineering applications involving cyclic loading is still not well understood due to the scarcity of fatigue and fracture toughness data. In general, the fatigue strength of as-built AM alloys is low due to the inherent defects, the heterogeneous microstructure and surface roughness of AM metal parts.

It could be expected that the remnant porosity within the AM part does not change the yield strength much as long as the pore size is below a critical value. However, this may not be the case for fatigue properties. Besides, parts having high ductility may provide increased fatigue life by decreasing crack propagation rate through the grains. A comparison of fatigue strength with tensile strength and elongation properties are presented in Fig. 11 to clarify the aforementioned statement. This figure depicts that the fatigue strength does not necessarily increase with

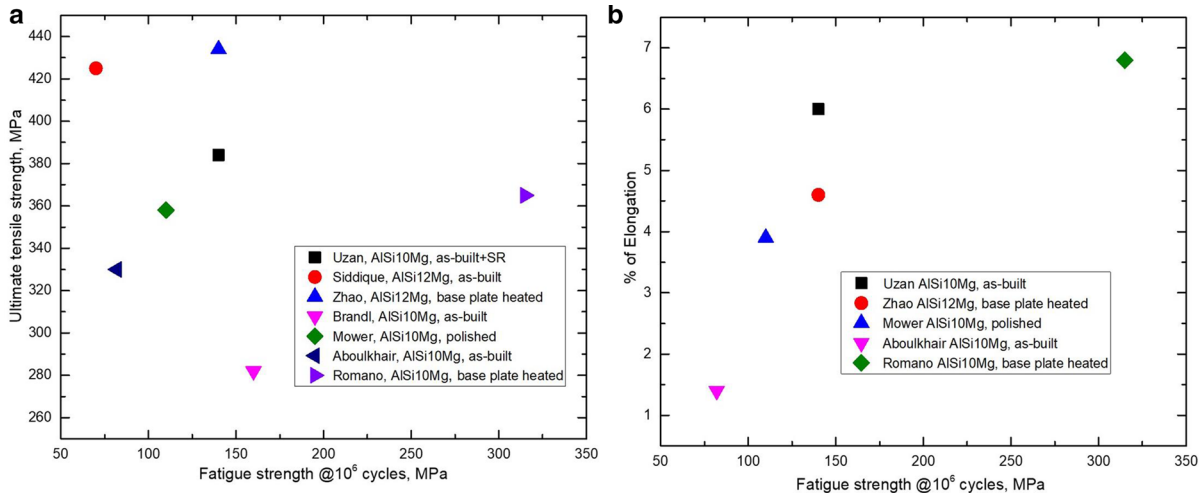

Fig. 11 Comparison of fatigue strength of L-PBF Al–Si–Mg alloy with **a** ultimate tensile strength, **b** % of elongation (data are from literature and re-plotted Aboulkhair et al. 2016b; Romano et al. 2018; Siddique et al. 2017; Uzan et al. 2017; Zhao et al. 2018))

tensile strength; however, there is a stronger relationship with ductility improvement.

However, a reasonable improvement in fatigue strength is found by changing process parameters or by applying a wide range of post-processing treatments. Therefore, the latter part of this paper will provide an overview of the fatigue properties of L-PBF produced AM alloys. This will contribute to the understanding of mechanical properties of innovative AM processed metals and will assist in identifying the best possible metal alloy for a specific application, e.g., in automotive or biomedical industry or any other future application.

4.1 Fatigue behaviour of Ti–6Al–4V alloy

Ti–6Al–4V has applications in biomedical, automobile, marine (Gorynin 1999), chemical (Gurrappa 2003), and aerospace industries (Boyer 1996), due to its high strength, corrosion resistance, and high fracture toughness properties (Liu and Shin 2019). It is a popular implant material because of its biocompatibility (Hao et al. 2016). Most implants are expected to have a lifetime of several decades; fatigue is an important consideration. Fatigue strength and related parameters (e.g., heat treatment, porosity fraction and surface condition) of L-PBF Ti–6Al–4V, which has been discussed in the following sections are compiled in Table 3.

4.1.1 Effect of porosity and roughness

The fatigue performance of AM Ti-alloy is hierarchically controlled by surface roughness, porosity and microstructure (Agius et al. 2018; Cao et al. 2018). Cao et al. (Cao et al. 2018) have given an insight on fatigue properties of Ti–6A1–4V alloys produced by E-PBF, L-PBF and LENS. According to their work, the L-PBF processed samples yield better fatigue strength (> 200 MPa) compared to the E-PBF (120–150 MPa) process. This is attributed to the high surface roughness (nearly 27 µm) associated with the E-PBF process, which is almost double of L-PBF (about 12 µm) in as-built condition (Greitemeier et al. 2016). The higher roughness in the E-PBF process is due to the process conditions and layer thickness. However, both as-built L-PBF and E-PBF parts offer lower fatigue strength than wrought milled alloys owing to higher surface roughness (Agius et al. 2018; Palanivel et al. 2016) than wrought-milled alloys. As-built samples mainly fail due to surface defects and show multiple crack initiation sites. From Fig. 12, it is evident that the fatigue strength of L-PBF Ti–6Al–4V samples can be increased from 210 MPa in the as-built condition to 500 MPa in the polished condition. Chemically accelerated vibratory polishing (CAVP) (Witkin et al. 2019), electro-polishing, and shot-peening (Benedetti et al. 2018) reduce the surface roughness dramatically in L-PBF Ti–6Al–4V alloy. CAPV removes a thin surface layer making the surface

Table 2 Static tensile properties of L-PBF steel parts

Alloy	Hatch spacing (μm)	Process condition	Build orientation	Yield strength (MPa)	Tensile strength (MPa)	% of elongation	Porosity (%)	References
PH1	100	Precipitation Hardening (400 °C)	XY	1297 ± 1.01	1450 ± 2.06	12.536 ± 1.07	< 1	Rafi et al. (2013b)
			Z	1100 ± 38.79	1467 ± 17	14.92 ± 0.32		
PH1	–	Peak aged condition	–	1170	1310	–	–	Rafi et al. (2013b)
18Ni (300) MS	105	As-built	XY	768.0 ± 29	1260.1 ± 79	13.9 ± 02	–	Suryawanshi et al. (2017b)
			Z	825.9 ± 96	1324.7 ± 51	14 ± 1.5		
		Aging (5 h at 480 °C)	XY	1953 ± 87	2216.1 ± 156	3.1 ± 0.4		
			Z	1833.3 ± 65	2088.3 ± 190	3.2 ± .0.6		
316L Stainless Steel	–	As-Built	XY	565	462	53.7	–	Riemer et al. (2014)
		Heat-treated (2 h at 650 °C)		595	443	48.6		
		Cast		530–680	220	> 40		
15-5PH (H900)	190	Heat-treated 1 h at 482 °C in air	–	1100	1470	15	–	Wegener et al. (2013)
		Handbook		1170	1310	10		
316L	–	Net shaped	–	640	760	30	–	Spierings et al. (2011)
		Handbook		310	620	30		
18Ni-3000	100	As-built	XY	900–1050	1010–1100	8.3–12.1	–	Hermann Becker and Dimitrov (2016)
			Z	1040–1080	1120–1205	12.0–12.1		
		Solution annealing (1 h at 830° C)	XY	800–810	950–1000	11.8–11.9		
			Z	800–815	950–990	12.5–13.5		
		Aging (6 h 490° C)	XY	1720–1790	1800–1840	5.1–7		
			Z	1750	860–1850	4.4–4.5		
17–4 PH	50	As-built	XY	650	1060	14.5	0.3	Yadollahi et al. (2017)
			Z	580	940	5.8	0.2	
		Heat-treated	XY	1250	1410	11	–	
			Z	1020	1150	2.8	–	

SR stress relief, *PH* preheating, *HIP* hot isostatic pressing, *T6* solution heat-treatment, *XY* the long axis of the specimen is parallel to the built platform, *Z* the long axis of the specimen is perpendicular to the build platform

Table 3 Fatigue parameters of L-PBF Ti–6Al–4V alloy

Variable parameter		Post Process condition	Microstructure	Surface roughness (μm)	Porosity (%)	Stress Ratio (R)	Fatigue strength @10^7 Cycles	References
–		SR (4 h at 650 °C)	α′ martensite	–	–	0.1	550	Rafi et al. (2013b)
–		Polished + SR (3 h at 650 °C)	Ultrafine lamellar α + α′ in prior β	–	–	− 1	360	Wycisk et al. (2015)
		Polished + HIP (4 h at 900 °C @1000 bar)	fine α + β lamellae and α needle	–	–	0.1	680	
						− 1	575	
		As-built + SR (3 h at 650 °C)	Ultrafine lamellar α + α′ in prior β	–	–	0.1	210	Wycisk et al. (2014)
		Polished + SR (3 h at 650 °C)					500	
Scan speed (mm/s)	960	–	α′ martensite	–	0.45	0.1	400	Gong et al. (2015)
	450				1.37		350	
	400				5.23		–	
	1260				1.37		–	
	1500				5.48		100	
–		As-built + HIP	Elongated primary α grain in β matrix		0.012	− 1	200	Kasperovich and Hausmann (2015)
		Machine + HIP					350	
Energy Density (J/mm^3)	33.74	Machined + preheating (200 °C)	Course lamellar α + β	–	–	0.1	–	Xu et al. (2015)
	50.62		Ultrafine lamellar α + β				400	
–		HIP (2 h at 920 °C @100 MPa)	fine α + β lamellae and α needle	–	–	− 1	620	Leuders et al. (2013)
–		As-built	α′ martensite	32	–	− 0.2	–	Edwards and Ramulu (2014)
		Machined		0.89			200	
–		Annealed (2 h at 710 °C)	α′ martensite	13	–	− 1	200	Greitemeier et al. (2016), Greitemeier et al. (2017), Melz et al. (2015)
		Milled + annealed (2 h at 710 °C)		109.9			475	
		HIP (2 h at 920 °C 100Mpa)		–			175	
		Milled + HIP (2 h at 920 °C 100 MPa)		–			600	

Table 3 continued

Variable parameter	Post Process condition	Microstructure	Surface roughness (µm)	Porosity (%)	Stress Ratio (R)	Fatigue strength @10^7 Cycles	References
–	As-built	–	6.83	0.35	− 1	275	Benedetti et al. (2018)
	Annealed (2 h at 920 °C)		–	–		250	
	Shot-peened		3.36	0.35		400	
	Electro-polished		0.54	–		300	
	HIP (2 h at 920 °C 100 MPa)		5.07	0.05		450	

defects rounder and improving the fatigue strength by around 70 ∼ 140 MPa, as listed in Table 3. Shot peening and electro-polishing also reduce the overall porosity fraction along with roughness, as these processes are more effective in changing the pore density near the surface.

However, the polished samples can still show significant scatter (Fig. 12) due to the presence of porosity (Wycisk et al. 2014; Zhao et al. 2016). Similar scatter in the S–N curve is observed by Benedetti et al. (2018), Tammas-Williams et al. (2017) and Gong et al. (2014a, b) for polished L-PBF Ti–6Al–4V alloy due to the presence of porosity.

The overall density of L-PBF Ti–6Al–4V is reported to be around 99.7–99.9% (Leuders et al. 2013; Thijs et al. 2010), whereas the highest reported density for the E-PBF process is 99.88% (Wang et al. 2016). The remaining porosity within the part causes fatigue failure of polished samples from sub-surface or internal defect as well as shows large scatter in the S–N curve. A variation in fatigue life associated with part density is mainly due to the change in scan speed. The part produced with optimum scan speed (960 mm/s) offers less internal porosity; hence a higher number of fatigue cycles (Gong et al. 2014a, b). Fatigue life can be further improved (250–300) MPa after applying the various post-heat treatment on the polished sample (Benedetti et al. 2018; Greitemeier et al. 2017; Wycisk et al. 2014), which reduces internal porosity. Therefore, these studies attributed fatigue life to crack formation and suggested that a reduced number of pores delays crack initiation. However, defect size and location are also detrimental factors for fatigue crack growth. Surface defects of AM produced material have more severe effects on fatigue life, as the stress intensity factor is higher for surface pores compared to internal pores (Murakami 2002).

The fatigue fracture surface analysis showed that crack initiation occurs mostly from the pores near the surface and fatigue life is more influenced by pore size, and aspect ratio compared to the overall pore volume (Tammas-Williams et al. 2017).

4.1.2 Effect of heat treatment

The effect of changes in pore morphology and surface roughness on fatigue life due to the application of a wide range of heat treatments have been reported

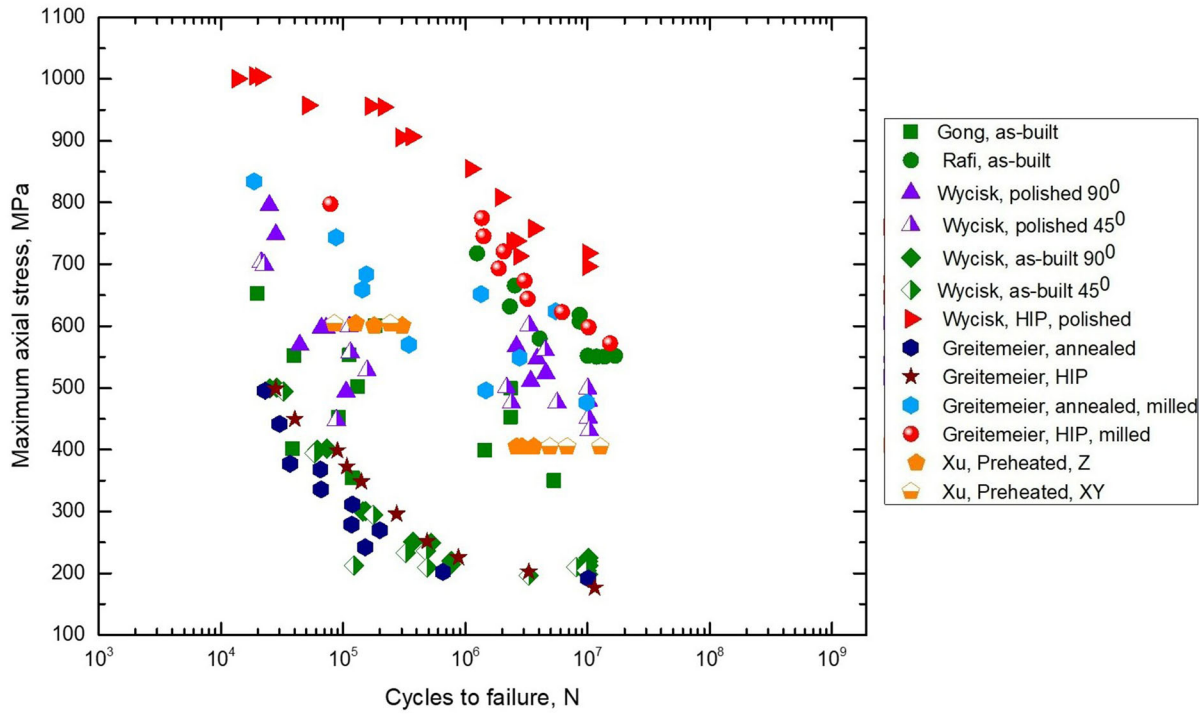

Fig. 12 Comparison of fatigue life of L-PBF produced Ti–6Al–4V alloy at different conditions for stress ratio, $R = 0.1$ (Data are from literature and re-plotted Gong et al. 2015; Greitemeier et al. 2017; Rafi et al. 2013b; Wycisk et al. 2014; Xu et al. 2015))

(Benedetti et al. 2018; Günther et al. 2017; Wycisk et al. 2015; Xu et al. 2015). Influence of these parameters on fatigue strength can be seen from Figs. 12 and 13. The heat treatment of the Ti-alloy, for instance holding 3 h at 6500 °C, helps reduce the lack of fusion defects as well as the amount of scatter in the S–N curve (Wycisk et al. 2014). However, reviewing this data indicates that HIP has a beneficial effect for fatigue strength of Ti–6Al–4V, as it has the potential to reduce internal porosity (Qiu et al. 2013) and improve fatigue life (Edwards et al. 2013). For example, a porosity content of about 0.35% in the as-built condition can be reduced to less than 0.05% by HIP treatment (Benedetti et al. 2018). Improvement in fatigue strength of about 300–350 MPa (Günther et al. 2017; Wycisk et al. 2015) from as-built condition to the HIP condition has been found in the literature (Benedetti et al. 2018; Facchini et al. 2009; Günther et al. 2017; Mower and Long 2016; Wycisk et al. 2015, 2014) HIP generally improves fatigue life by closing sub-surface pores, however, may lead to higher surface roughness by coarsening of the microstructure (Facchini et al. 2009; Mall et al. 2004) and increasing α-lamella thickness (Mower and Long 2016). This increased surface roughness may supersede the effect of reduced internal defects on fatigue strength from HIP (Greitemeier et al. 2016). Therefore, Greitemeier et al. (2016, 2017) suggested machining after HIP as the best approach to improve fatigue life, which has also been confirmed by Kasperovich and Hausmann (2015) and Masuo et al. (2018). However, the test results from Edward and Rumulu (2014) do not support this hypothesis. However, these authors used different stress ratios in fatigue testing and hence, no direct comparison can be drawn. Moreover, the fatigue strength of HIP samples from Benedetti et al. (2018) is significantly lower than those of the HIP samples from Wycisk et al. (2015). Different test frequency or duration of heat treatment (Table 3) can be reasons for this high scatter.

4.1.3 Very high cycle fatigue strength

Günther et al. (2017) and Wycisk et al. (2015) explored the relative effects of surface and internal defects under very high cycle fatigue, as shown in

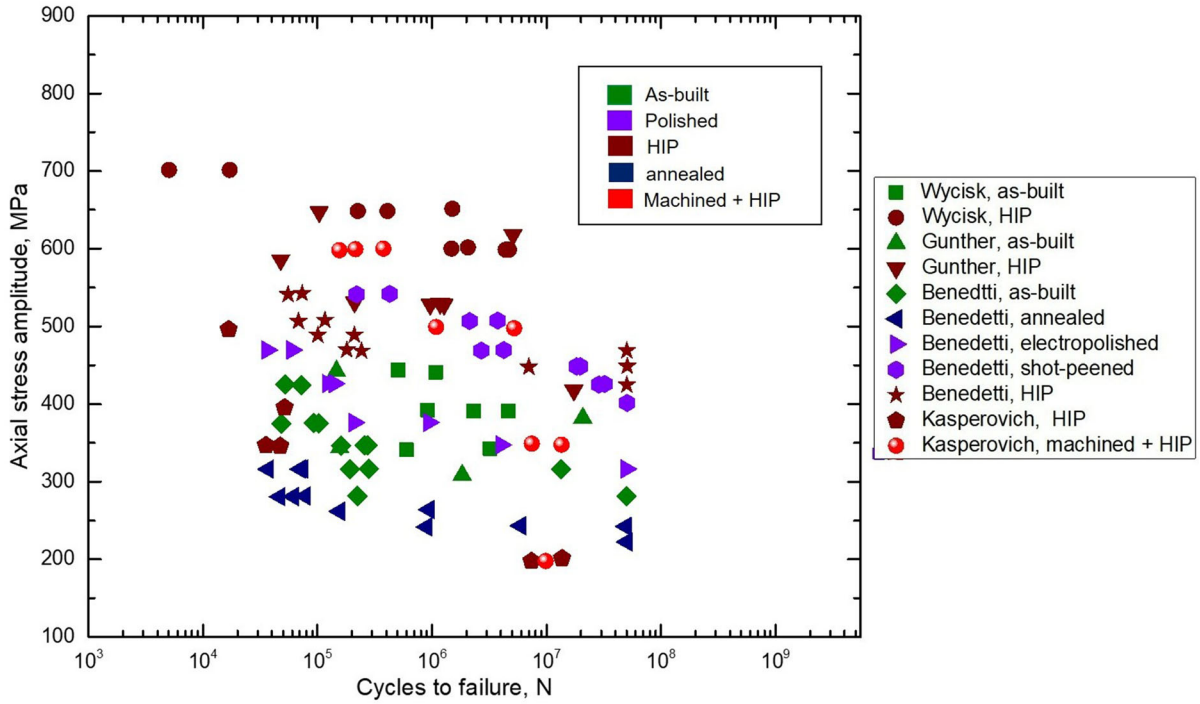

Fig. 13 Comparison of fatigue life of L-PBF produced Ti–6Al–4V alloy tested at fully reversed conditions $R = -1$. (Data are from literature and re-plotted Benedetti et al. 2018; Günther et al. 2017; Kasperovich and Hausmann 2015; Wycisk et al. 2014))

Fig. 14. The crack initiation started from internal defects instead of the surface defects for the very high cycle regime (around 10^9 cycles). This crack initiation transition occurs at higher cycles ($> 10^7$ cycles) for the wrought material (Furuya and Takeuchi 2014), while it occurs in L-PBF Ti–6Al–4V alloy at around 10^7 cycles for tension–compression loading and at greater than 10^6 cycles for tension-tension loading (Wycisk et al. 2014). However, crack initiation at lower cycles can also be from internal pores instead of surface pores if the volume of internal porosity is very high, which reduces crack nucleation time (Holmes and Queeney 1985). Crack initiation primarily depends on crack size at low-stress levels, however, at high-stress levels, surface defects dominate as the stress around these leads to exceeding the crack growth threshold value (ΔK_{th}) (Cao and Ravi Chandran 2017). Therefore, to improve the fatigue life of L-PBF Ti–6Al–4V alloy it is important to study crack growth properties as crack initiation has a negligible impact on the fatigue life.

4.1.4 Anisotropy effect

Build orientation causes anisotropy in the mechanical property of AM materials (Cao et al. 2018). This level of anisotropy is higher for as-built samples (Riemer et al. 2014), and the post-processing techniques like HIP considerably reduce this (Riemer et al. 2014). The Z-direction (vertical) build shows the weakest mechanical properties, which is almost 8–11% lower than the X–Y orientation (Chastand et al. 2018; Edwards and Ramulu 2014; Frazier 2014). Yadollahi et al. (2017) proposed that reason for this anisotropy is the orientation of the LOF pores. LOF pores occur in between layers and are more detrimental for vertical samples due to the loading orientation, thus reducing mechanical properties. In as-built condition α' martensitic phase (as mentioned in Sect. 2.3.1) is aligned along the build direction due to high temperature gradient. Upon heat treatment, α' martensitic phase transforms into uniform lamellar α + β microstructure, with no significant grain orientation (Wauthle et al. 2015). This can be a reason that heat-treated samples show less or no anisotropy effects. In contrast, Wycisk et al. (2015) have reported that build

orientation has no significant effect on fatigue properties even in as-built condition. This contrast can be due to the use of different process parameters and associated part density.

4.1.5 Crack growth behaviour of Ti–6Al–4V alloy

From a damage tolerance point of view, it is highly desirable to have a high crack growth threshold (ΔK_{th}) value to reduce the crack growth time. However, the finer α-grain microstructure of Ti–6Al–4V makes the critical defects sensitive to cyclic loading, leading to a low value of ΔK_{th} even if the material shows higher axial fatigue strength (Lucas and Konieczny 1971). Fatigue crack growth (FCG) resistance performance of L-PBF Ti-6A1-4 V for specific defects like surface roughness and pores (Greitemeier et al. 2017; Read et al. 2015; Witkin et al. 2019; Zhai et al. 2015) is summarized in Table 4. FCG resistance for as-built L-PBF Ti–6Al–4V alloy is very low and insufficient, which is about 10–20% (Fatemi et al. 2017; Sterling et al. 2016) of the wrought materials and does not improve even after machining or annealing. This is due to the finer microstructure and smaller grain size of additively manufactured Ti–6Al–4V, which promotes crack propagation through the small grains once the crack is initiated from one grain by releasing the plastic zone (Cao and Ravi Chandran 2017). An increase in ΔK_{th} value with increase in α-lath thickness for AM Ti–6Al–4V is reported in the literature (Galarraga et al. 2017; Greitemeier et al. 2017; Wycisk et al. 2014; Zhai et al. 2015). A gradual heat treatment may lead to coarsening of grains and reduction in residual stress which increases ΔK_{th} value (Leuders et al. 2013). HIP of L-PBF Ti–6Al–4V increases ΔK_{th} over the wrought material (Cao et al. 2018; Tammas-Williams et al. 2017) as the coarsening effect on microstructures increases the ductility. An increase in the ΔK_{th} after HIP compared to annealed ($\sim$ 3 MPa $\sqrt{m}$) condition for L-PBF Ti-6A1-4 V is shown in Fig. 15b. Wycisk et al. (2014) obtained a slightly improved ΔK_{th} value of 3.5 MPa $\sqrt{m}$ for annealed Ti–6Al–4V compared to literature ($\sim$ 3 MPa$\sqrt{m}$) (Cao et al. 2018; Edwards and Ramulu 2014; Tammas-Williams et al. 2017). Leuders et al. (2013) reported higher ΔK_{th} value for cracks growing parallel to the

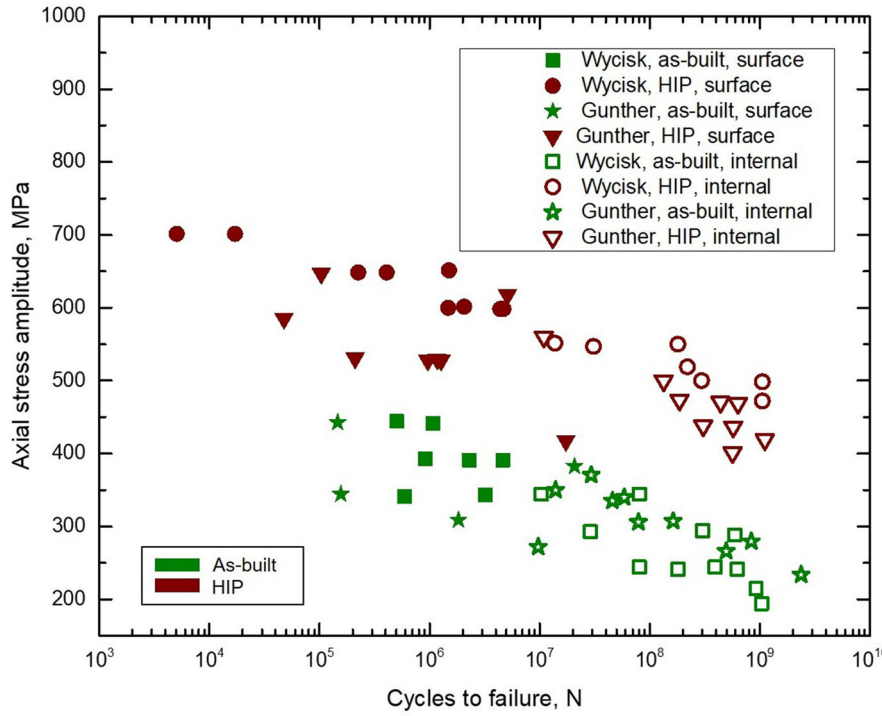

Fig. 14 Comparison of surface and sub-surface defects on fatigue life of L-PBF Ti–6Al–4V at $R = 0.1$ (data from literature and re-plotted Günther et al. 2017; Wycisk et al. 2015))

Table 4 FCG threshold values for Ti–6Al–4V alloy

AM process	Process condition	Orientation	Test type	Crack growth threshold (ΔK_{th})	References
DMLS	Annealed	–	K-decreasing, R = 0.1	3.2	Greitemeier et al. (2017)
	HIP			4.4	
E-PBF	Annealed	–	K-decreasing, R = 0.1	4.2	Greitemeier et al. (2017)
	HIP			4.8	
L-PBF	HIP	*CD* ⊥ *BD*	–	4.2	Riemer et al. (2015)
		CD ∥ *BD*		4.4	
	Annealed (@800 °C)	*CD* ⊥ *BD*		4.4	
		CD ∥ *BD*		4.4	
	Annealed (@1050 °C)	*CD* ⊥ *BD*		3.8	
		CD ∥ *BD*		5.3	
L-PBF	AS-built	*CD* ⊥ *BD*	K-decreasing, R = 0.1	1.4	Leuders et al. (2013)
		CD ∥ *BD*		1.7	
	HIP	*CD* ⊥ *BD*		3.8–4.2	
		CD ∥ *BD*		4.2	
	Annealed (@800 °C)	*CD* ⊥ *BD*		3.8–4.2	
		CD ∥ *BD*		3.7	
	Annealed (@1050 °C)	*CD* ⊥ *BD*		3.8–4.2	
		CD ∥ *BD*		6.1	
L-PBF	Annealed (@650 °C)	*CD* ⊥ *BD*	K-decreasing, R = 0.1	3.48	Wycisk et al. (2014)

CD crack direction, *BD* build direction

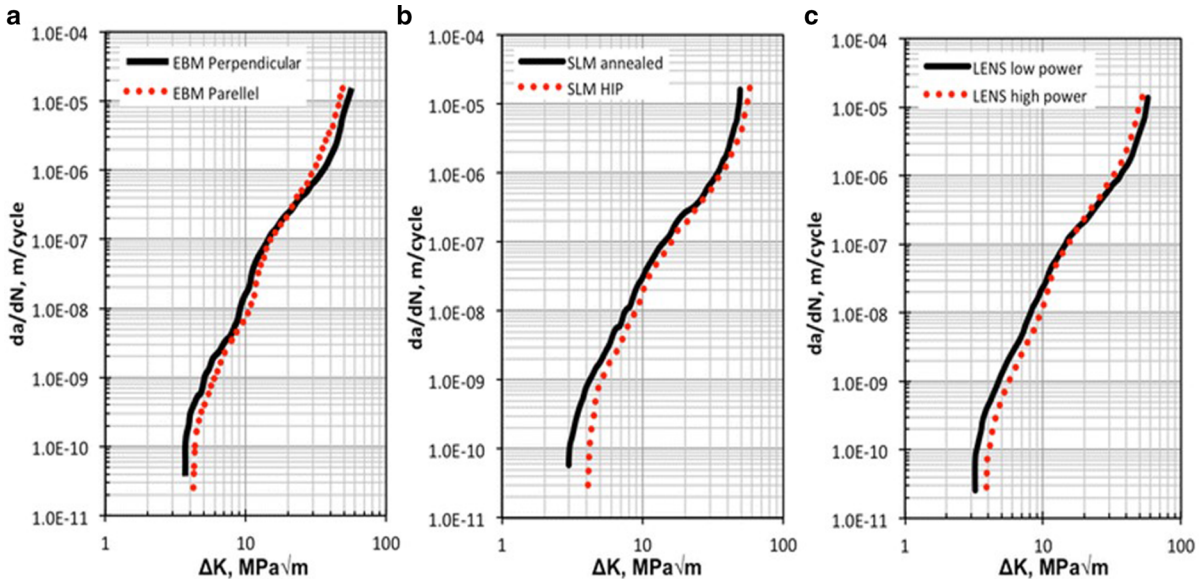

Fig. 15 FCG curve of Ti–6Al–4V showing the effect of **a** build orientation, **b** heat treatment, and **c** process parameter (Cao et al. 2018)

build direction. Similar anisotropy effect is observed in E-PBF Ti–6Al–4V by Galarraga et al. (2017), as shown in Fig. 15a. Although applying the same post-processing parameters as Leuders et al. (2013), Riemer et al. (2015) found no anisotropy effect on ΔK_{th} value (Table 4) except in the as-built condition. However, a slight increase in threshold has been reported after high-temperature annealing by both the authors.

Greitemeier et al. (2017) have shown that the E-PBF process produces a higher ΔK_{th} of Ti–6Al–4V than direct metal laser sintering (DMLS) in the annealed condition. Internal defects is a reason of low ΔK_{th} in DMLS condition. However, in the Paris regions of FCG curves, no significant differences in crack growth properties are found between annealed and HIP material (Greitemeier et al. 2017). In this region, fatigue properties seem to be similar for all the processes and heat treatments, as shown in Fig. 15b.

Process parameters also affect crack growth properties. Figure 15c shows a higher ΔK_{th} value of Ti–6Al–4V built at high energy density compared to low energy density because of the reduced LOF pores (Zhai et al. 2015). Therefore, optimized machining, melting strategy, laser power and other process parameters are preferable to avoid formation of defects and hence to increase FCG resistance (Agius et al. 2018; Gong et al. 2014a, b).

Overall, fine-grained Ti-alloy shows higher fatigue strength. However, the fine microstructure shows an opposite effect on crack initiation (reduces) and propagation behaviour (increases), therefore may produce low threshold value (Li et al. 2018).

4.2 Fatigue behaviour of Al–Si–Mg alloy

Aluminium (Al) alloys are applicable to many engineering applications because of its lightweight and high corrosion resistance properties. AM processed Al materials can outperform conventionally fabricated Al alloys in terms of static strength (Herzog et al. 2016; Trevisan et al. 2017); however, the inherent porosity and surface imperfections of AM parts are detrimental to fatigue performance. In order to ensure the quality and integrity of the AM structural parts, a rigorous mechanical investigation is often warranted, which could be costly and time-consuming. The literature data concerning L-PBF Al alloys' fatigue performance is very limited so far, which are listed in Table 5.

4.2.1 Role of surface roughness

It is important to note that the reported fatigue properties of L-PBF Al alloy are lower than that obtained by the conventional processing in as-built condition. This low fatigue life in the as-built state is attributed to the high surface roughness of AM parts due to unmelted powder at the periphery (Stephens et al. 2000; Yadollahi and Shamsaei 2017). The surface roughness of as-built AM parts leads to rapid crack initiation and propagation as surface defects impart higher stress compared to internal defects (Murakami 2002). Cracks for as-built samples can also propagate from sub-surface pores due to the presence of residual stress associated with the L-PBF process. Machining or polishing is recommended to improve (Aboulkhair et al. 2016a; Beevers et al. 2018; Mower and Long 2016; Uzan et al. 2017) fatigue strength as compared to as-built samples by reducing roughness (Uzan et al. 2017). However, the improvement in fatigue life after machining is not consistent among various work in literature. Uzan et al. (2017) claimed a significant improvement in fatigue strength of as-built samples after machining, Mower and Long (Mower and Long 2016) confirmed a similar increase in fatigue strength after polishing. Aboulkhair et al. (2016a) found no significant improvement in fatigue strength of as-built samples after machining (Fig. 16). However, the authors claimed that machining after T6 heat treatment almost doubled the fatigue strength.

Like Ti-alloy, the pore morphology of the AlSi10Mg alloy can be modified after shot-peening (Damon et al. 2018). Shot peening reduces the surface roughness by increasing the sphericity of near-surface pores. Damon et al. (2018) found around 20 MPa increase in fatigue strength for shot peening of AlSi10Mg compared to as-built samples, with all other processing conditions being the same.

The magnitude of surface roughness of as-built parts depends on scanning strategy as well, such as contouring. Contouring is a scanning strategy where a boundary scan (outer circle for round fatigue sample) is performed, followed by inner hatch filling for solid material. Samples produced without contour (boundary scanning) show less average roughness, and provide similar fatigue strength as milled samples (Beevers et al. 2018). On the other hand, samples with contour scanning (boundary scanning) show early failure provided that having higher roughness value, as

Table 5 Fatigue data of L-PBF Al-alloy

Alloy	Hatch spacing (μm)	Process condition	Build orientation	Surface roughness (μm)	Porosity (%)	Stress ratio (R)	Fatigue strength @10^7	References
AlSi10Mg	200	Machined	Z	1.750	0.025	− 1 (rotating bending)	125	Uzan et al. (2017)
		Machined + polished		0.587	0.025		125	
		SR (2 h at 300 °C)		–	0.054		75	
		HIP (250 °C) + machined + polished		0.520	0.048		75	
		HIP (500 °C) + machined + polished		0.490	0.014		–	
AlSi10Mg	100	As-built	XY	4–5	–	− 1	50	Mower and Long (2016)
			Z				50	
		Polished	XY	1.5			80	
	–	As-built	–	17.1	–	0.1	–	Aboulkhair et al. (2016a)
		Machined		0.62			63	
		T6 (1 h at 520° C + 6 h at 160 °C)					94	
		Machied + T6					126	
	–	Preheating (200 °C) + 60 μm layer thickness	Z	0.33	0.64	− 1	150	Romano et al. (2018)
		Preheating (165 °C) + 30 μm layer thickness			–		240	
	–	Vibratory finished	Z	3	0.03	− 1	fails@10^5	Beevers et al. (2018)
		Vibratory finished(w/o contour)		0.7	0.04		120	
		Milled		0.3	–		120	
	–	As-built	XY	–	0.5–1.1	− 1	75	Damon et al. (2018)
		Shot-peened			0.1–0.3		80	
AlSi12Mg	190	As-built + SR (2 h at 240 °C)	XY		0.25	− 1 (compression-tension)	65	Siddique et al. (2017)
		PH (200 °C) + SR (240 °C)			0.12		100	
	190	PH at 200 °C	XY	–	0.4–1.6	0.1	130	Zhao et al. (2018)
			Z		0.2–1.3		140	
	–	As-built (single melt)	XY	–	–	0.1	60	Suryawanshi et al. (2016)
		Heat-treated (single melt)					110	
		As-built (checker-board)					70	

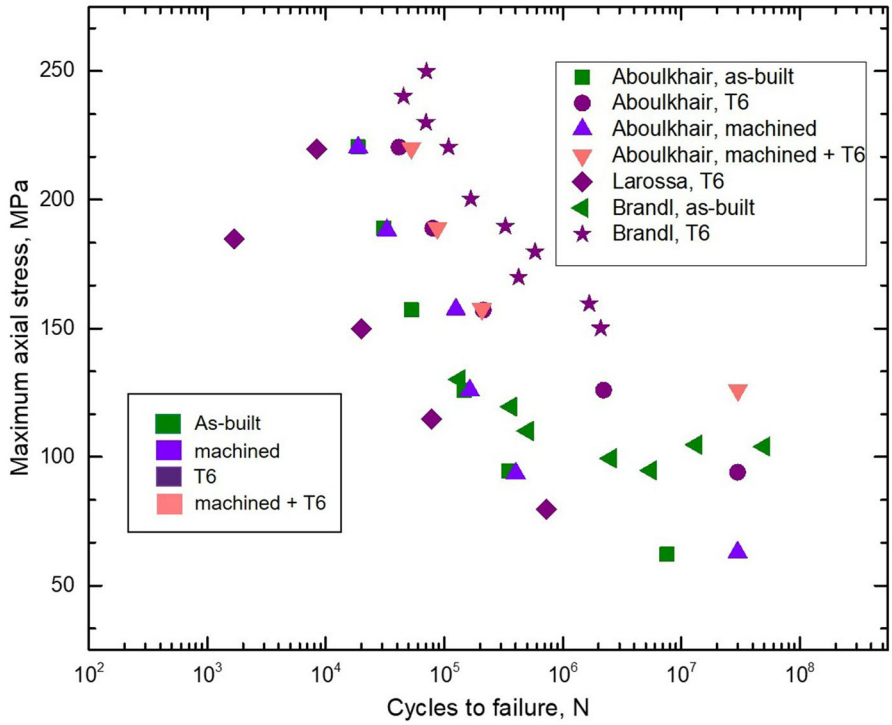

Fig. 16 Fatigue strength of L-PBF AlSi10Mg alloy for machined and heat-treated conditions (data from literature and re-plotted) (Aboulkhair et al. 2016a; Brandl et al. 2012; Larrosa et al. 2018), $R = 0.1$

shown in Table 5. A similar conclusion is drawn by Brandao et al. (2017). Nevertheless, microstructure and hardness properties are not affected by the contour scanning strategy. Compressive residual stress is generated when producing samples without contouring which is attributed as a contributor to improved fatigue performance. Beever et al.'s (2018) results also showed that milling is beneficial over vibratory finishing to improve the surface quality and fatigue life for AlSi10Mg. To summarise, surface quality plays an important role in fatigue life. All sorts of surface processing seem to improve fatigue life in Al-alloy, although the magnitude of improvement varies depending on other variables (machine parameter or heat treatment).

4.2.2 Pre-heating and post heat treatment

The Al-samples built with pre-heated platform showed a higher fatigue resistance than those produced at room temperature (Brandl et al. 2012; Siddique et al. 2017). Siddique et al. (2017) investigated for defect distribution, and the authors found that samples with base plate heating have less porosity (013–0.29%) compared to the ones without base plate heating (0.26–0.38%). The fatigue performance is consequently higher for samples with base plate heating, as shown in Fig. 17. A decrease in the temperature gradient causes a reduction in porosity due to base plate heating. Besides, baseplate-heated samples have higher crack growth resistance due to coarsening of the microstructure by forming elongated grains. Siddique et al. reported about 45% higher fatigue strength at 109 cycles for samples with base heating compared to those without base plate heating, (Siddique et al. 2015). For a very higher number of cycles (> 107), the smaller embedded pores start to contribute to crack initiation. Therefore, samples with comparatively higher porosity without base plate heating leads to early failure.

Uzan et al. (2017) assessed the effect of different post-processing heat treatments, such as stress relief, surface polishing and HIP treatment for samples produced without base plate heating. The average part density was found to be lower for stress relieved samples (2.616 g/cm^3) compared to the as-built (2.622 g/cm^3) samples due to the temperature effect that introduces thermally induced pores (TIP). In contrast, the samples that have been both stresses relieved and HIPed show the highest density (2.645 g/

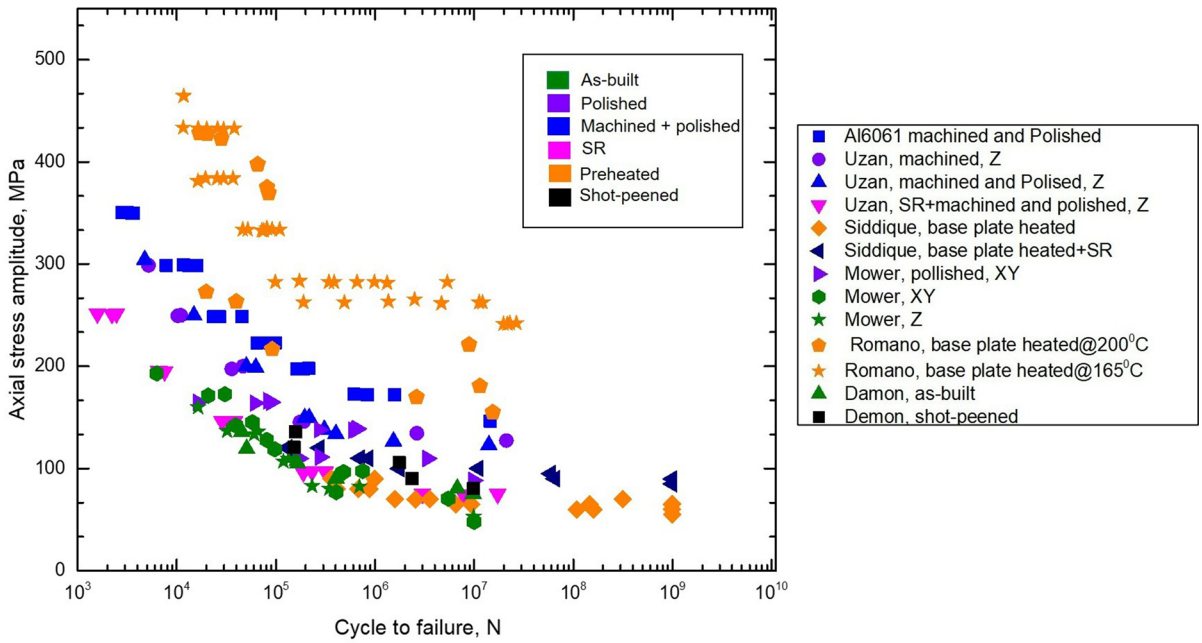

Fig. 17 Fatigue strength of L-PBF AlSi10Mg alloy in different processed conditions ($R = -1$) (data from literature and re-plotted) ("ASTM B85-03, Standard Specification for Aluminum-Alloy Die Castings"; Damon et al. 2018; Larrosa et al. 2018; Mower and Long 2016; Romano et al. 2018; Siddique et al. 2017; Uzan et al. 2017)

cm^3) compared to other conditions, and the part density increases with an increase in the HIP temperature. Nevertheless, the fatigue resistance, hardness, fracture toughness, and yield stress values are the lowest for the stress relieved, and the HIP treated part. At the same time, these properties are comparatively higher for samples which have been machined after heat treatment. The authors (Uzan et al. 2017) have claimed that prolonged heat treatment during stress relief and HIP causes the precipitation of Si particles from the alloy, which in turn increases the surface roughness. Similar to Uzan et al. (2017), a significant reduction (23%) in porosity is observed after applying both stress relief and HIP treatment by Larrosa et al. (2018). According to Larrosa et al. HIP samples survived 63,000 more cycles than as-built condition, which is contrary to the finding of Uzan's study.

Like Base-plate heating, Peak-hardening is also found to positively affect the fatigue strength of Al-alloys in many studies (Aboulkhair et al. 2016a; Bagheri et al. 2018; Brandl et al. 2012; Siddique et al. 2017). Brandl et al. (2012) found significant improvement in fatigue strength for peak-hardened (T6) samples with or without platform-heated. However, the authors recommended the T6 on platform-heated (300 °C) samples as the best approach to enhance the fatigue resistance. Like Brandl et al. (2012), Bagheri et al. (2018) obtained a considerable increase in fatigue strength after T6 treatment, though T6 samples reveal higher porosity than as-built samples. Aboulkhair et al. (2015) mentioned both T6 and machining to improve fatigue life separately, although the effect is true only for low-stress level. Hence the authors reported machining after T6 as the most effective procedure to improve fatigue property, although the corresponding fatigue strengths obtained (Aboulkhair et al. 2016a) at 10^7 cycles are lower than that of the findings of Brandl et al. (2012). However, T6 does not significantly improve fatigue strength in Larrosa et al.'s (2018) study compared to other published work.

Post-processing treatment on L-PBF AlSi10Mg alloy is not consistent among several available studies. Table 6 shows the relative improvement in the fatigue life of Al-alloy after heat treatment as found in the literature.

Table 6 Effect of different heat-treatment on porosity and fatigue strength of L-PBF Al-alloy

Type of heat-treatment	% of porosity	Surface roughness	Fatigue strength	Critical stress intensity	References
T6	↓	–	↑↑	–	Aboulkhair et al. (2016a), Maskery et al. (2015a)
HIP + T6	↓↓	–	↑	–	Larrosa et al. (2018)
PH + T6	↓	–	↓	–	Beevers et al. (2018)
	↓	–	↑↑↑	↑	Brandl et al. (2012)
SR + T6	↓	–	↑	↓	Siddique et al. (2017)
T6	↑	–	↑	–	Bagheri et al. (2018)
HIP	↓	↑	↓	–	Uzan et al. (2017)

T6 peak-hardening, HIP: hot isostatic pressing, *SR* stress relief, *PH* platform heating, ↑ increasing, ↓ decreasing

4.2.3 Porosity and machine parameters

Porosity is one of the key reasons for fatigue failure. From the previous section, it can be seen that heat treatment reduces porosity and improves fatigue life, the effect of which is not consistent. However, the formation of porosity is regulated by various machine parameters; therefore, optimisation of these parameters can improve fatigue life in Al-alloy by reducing porosity. According to Beevers et al. (2018), a slight change in AM layer thickness can affect the defect population, which makes the fatigue properties comparable to conventional manufacturing without any post-processing. Brandao et al. (2017) also reported a similar effect of layer thickness on fatigue properties. Romano et al. (2018) reported a significant reduction in porosity (as shown in Table 5) by changing layer thickness, which improves the fatigue strength $\sim$ 90 MPa.

Laser power also directly controls defect formation and fatigue. Low laser power leads to the formation of LOF pore, which can reduce fatigue strength, as seen in the work by Mower and Long (2016). Furthermore, Romano et al. (2018) has reported a higher fatigue strength compared to conventional processing using a laser power almost 50% higher than other studies (Mower and Long 2016; Siddique et al. 2017; Uzan et al. 2017). Reduction in porosity depends on hatch spacing as well. Tang and Pistorius (2017) observed that multiple melting zones associated with lower hatch spacing (0.16 mm) reduce lack of fusion pores, thus providing better fatigue strength.

4.2.4 Effect of build orientation

Like Ti, vertical samples have lower fatigue life than horizontal samples in Al-alloy. Nevertheless, build orientation is found to have an effect on samples produced at room temperature without applying any pre-and post-heat treatment (Awd et al.). Both base plate heating (Zhao et al. 2018) and peak hardening (Brandl et al. 2012) remove the build orientation effect by minimizing the thermal gradient along the build direction. To better understand the effect, variation in fatigue stress with build direction has been presented in Fig. 18 for AlSi10Mg alloy (Brandl et al. 2012; Larrosa et al. 2018; Zhao et al. 2018). However, it is worth noting that many works tend to omit the build orientation effect on fatigue life as this factor is often overshadowed by the effect of process parameters on fatigue life, which may vary up to 28% under fatigue loading (Romano et al. 2018).

4.2.5 Effect of gas pores and oxide pores

L-PBF Al-alloys usually contain a higher density of gas pores compared to Ti-alloys because of the solubility of H_2 in the melt pool and low solubility in the solid. Gas pores can initiate fatigue failure in AM Al-alloy if the volume fraction is very high. Zhao

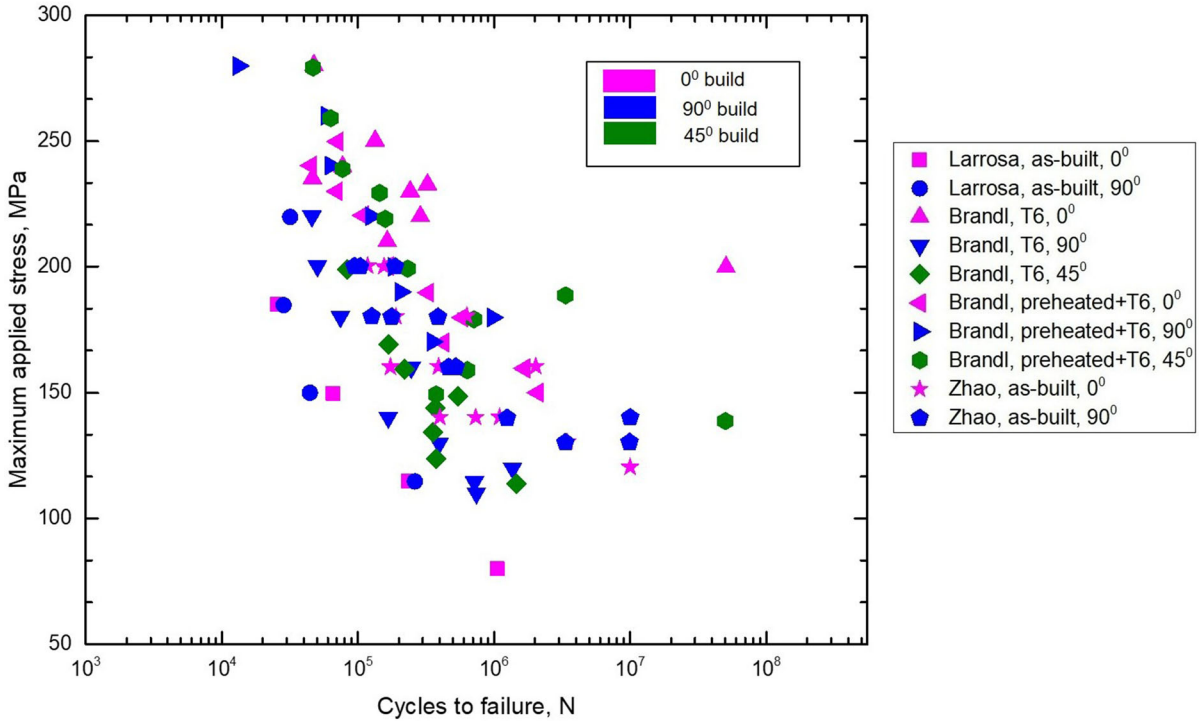

Fig. 18 Fatigue strength of L-PBF AlSi10Mg alloy at different build orientation (Data from literature and re-plotted) (Brandl et al. 2012; Larrosa et al. 2018)

et al. (2018) investigated the correlation between gas porosity and fatigue life, and found gas porosity having a volume fraction of 0.2–1.6% and average diameter of 20–55 μm for both (vertical and horizontal) directional builds. This study claims that the average pore size has more effect on fatigue life than porosity fraction, which agrees with the literature (Murakami 2002). Build orientation does not affect the density and size of gas pores. Unlike Zhao et al. (2018), Tang and Pistorius (2017) observed less gas porosity compared to LOF and have suggested gas pores are less problematic for fatigue failure. Instead, they found large oxide pores of different sizes. The presence of oxide particles, as well as unmelted powder, are higher in the L-PBF Al-alloy compared to other alloys because of the poor wetting capability of molten aluminium, which hampers part consolidation (Louvis et al. 2011). This phenomenon leads to anisotropy in fatigue strength as lack of fusion contributes more to the fatigue failure of the vertical sample.

4.2.6 Crack growth behaviour of Al–Si–Mg alloy

As discussed in the Titanium section, FCG is equally important as the S–N data. The S–N curve data in the previous section shows that fatigue properties of L-PBF processed parts are mostly dominated by surface roughness, porosity level and defect size instead of microstructure. However, FCG has been observed to be dependent on the grain size and orientation. Very few studies have focused on this property of an L-PBF Al-alloy. Romano et al. (2018) have conducted FCG tests for vertically built samples, and reported a crack growth threshold (ΔK_{th}) value of 3.2–3.6 MPa $\sqrt{m}$ which is within the traditionally cast material threshold bound 2.1–6.9 MPa $\sqrt{m}$ (Lados and Apelian 2004). However, the effect of build orientation, microstructure and post-treatment were omitted in this study. The effect of scan strategy and heat treatment on FCG of Al-12Si alloy is studied by Suryawanshi et al. (2016), as shown in Fig. 19. From Fig. 19, the ΔK_{th} value does not vary with as-built single melt (AS) and chessboard (CS) scan strategy in the as-built condition. Moreover, no anisotropy was

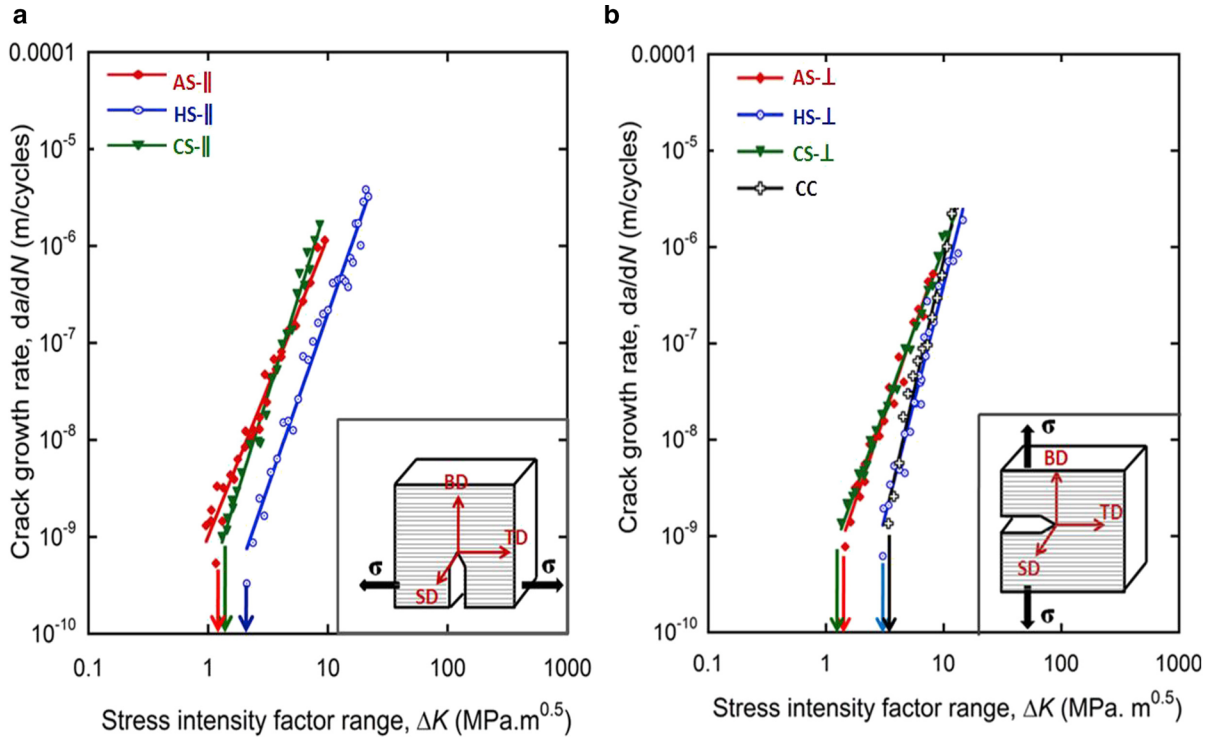

Fig. 19 FCG variation of AlSi-12 alloy for different process condition: **a** horizontal built, and **b** vertical built (Suryawanshi et al. 2016); where *AS* single-melt, *CS* chessboard, *HS* heat-treated single melt, *CC* conventional cast

observed for the ΔK_{th} value in the CS condition. However, a slightly higher threshold is recorded in the AS condition for crack growth perpendicular to the build direction. The authors have attributed scan direction (SD) as the reason for this anisotropy. Cracks perpendicular to build direction (BD) which are travelling along the scan overlap propagate is relatively direct, whereas, crack propagation perpendicular to SD (parallel to BD) is more tortuous.

Heat treatment (HS) increases the ΔK_{th} value for both the build directions (Suryawanshi et al. 2016). However, a slight anisotropy is found for the stress intensity factor range even in the heat-treated condition (Siddique et al. 2017; Suryawanshi et al. 2016). This contrasts with axial fatigue data, where heat treatment eliminates the anisotropy effect (Brandl et al. 2012). Siddique et al. (2017) also reported improvement in the threshold value after stress relief heat treatment for samples built with and without base plate heating. Base plate heating increases dendrite thickness (0.53 µm) compared to as-built condition (0.35 µm), which in turns delays crack growth due to coarsening of grain size. However, no effect of heat treatment is reported in the Paris region where crack size is more significant than grain size and independent of microstructure (Suresh 1998). This research has not studied the effect of build direction on crack growth properties (Table 7).

The above discussion has shown that L-PBF produced Al-parts present higher tensile but lower fatigue properties compared to conventional fabrication even in as-built condition (Trevisan et al. 2017). Like Ti-alloy, roughness and porosity are the critical reasons for fatigue failure in Al-alloy. Machining improves fatigue life, although it increases scatter in the S–N curve. Variation in fatigue life after machining happens due to the shifting of subsurface pores towards the surface in some cases. Unlike Ti-alloy, the fatigue strength improvement of Al-alloy is not significant after heat treatment. Furthermore, static mechanical properties may be degraded with heat treatment as it precipitates excess Si particles from α-Al, which is not desirable. Therefore, fatigue life improvement of Al-alloy with heat treatment yet requires extensive research efforts. Besides, surface quality and defects have a substantial impact on axial

Table 7 Fatigue crack growth threshold value of L-PBF Al-alloy

AM process/ alloy	Process condition	Orientation	Test type	Crack growth resistance (ΔK_{th})	References
L-PBF AlSi12Mg	SR	*CD* ∥ *BD*	K-decreasing, R = 0.1	3.2	Siddique et al. (2017)
	Base plate heated + _ SR			3.5	
L-PBF AlSi12Mg	As-built (Single Melt)/AS	*CD* ⊥ *BD*	K-decreasing, R = 0.1	1.4	Suryawanshi et al. (2016)
		CD ∥ *BD*		1.1	
	Heat-treated (4 h at 400 °C) (Single Melt)/HS	*CD* ⊥ *BD*		3.1	
		CD ∥ *BD*		2.0	
	As-built (Checkerboard)/CS	*CD* ⊥ *BD*		1.3	
		CD ∥ *BD*		1.3	
L-PBF AlSi10Mg	Preheating (200 °C) + 60 µm layer thickness	*CD* ∥ *BD*	(K-decreasing) R = 0.7 (constant amplitude) R = − 1	3.2 3.6	Romano et al. (2018)

fatigue behaviour which is affected by various process parameters such as laser power, powder properties, hatch thickness, and build orientations. In L-PBF Al, a variety of machines and parameters are used to fabricate samples, which causes variability in part density and fatigue strength. As discussed in Sect. 4.2.3, optimization of process parameters significantly affects defect formation and fatigue life. Low-elongation is the other drawbacks of Al-alloy, which causes lower crack growth threshold property of long cracks. Furthermore, researchers have investigated the fatigue properties of Al-alloy using different L-PBF process parameters and machines therefore, it is not easy to compare the various results for making a general recommendation of the factors affecting fatigue and crack initiation, especially when the number of studies are still minimal.

4.3 Fatigue behaviour of stainless steels

Steel is one of the most widely used engineering materials owing to its high strength stiffness, and cost effectiveness leading to a wide variety of applications. Several types of steel can be successfully processed by L-PBF (Bajaj et al. 2020; Herzog et al. 2016), such as maraging steel (Kempen et al. 2011), 17-PH (Murr et al. 2012b; Wegener et al. 2013), AISI 316 (Leuders et al. 2014; Li et al. 2011; Riemer et al. 2014), and 15-5PH (Islam et al. 2013). About 35% of published AM metal alloy work has been undertaken for steel. A wide range of research has been carried out concerning the processes, microstructure evolution and static loading properties (Facchini et al. 2009; Kruth et al. 2012; Murr et al. 2012b; Rafi et al. 2013b; Yasa and Kruth 2011) of AM steel parts. Among the available studies of steel, fatigue properties of L-PBF produced samples (mostly stainless steels) are listed in Table 8. Like Ti and Al-alloy, as-built L-PBF steel demonstrates inferior fatigue properties compared to wrought counterparts because of its inferior surface condition. However, machined or turned samples almost doubles the fatigue strength, as a reduction of roughness value from 13 to 1 µm (Uhlmann et al. 2017), Table 8. Similar improvement in fatigue strength of 316L steel for machined and polished samples has been reported in many studies (Riemer et al. 2014; Spierings et al. 2011; Zhang et al. 2018a). Hence, L-PBF 316L and PH steel show comparable results with their conventional counterparts only after machining, as shown in Fig. 20.

L-PBF produced 316L steel reveals fewer build defects than any other Fe-based alloy and can provide at least 45% (Riemer et al. 2014) of the conventional HCF strength without any post-processing (Riemer

Table 8 Fatigue data of L-PBF fabricated steel parts

Alloy	Microstructure	Process condition	Build orientation	Surface roughness (μm)	Porosity (%)	Stress ratio, R	Fatigue strength @10^7	References
PH1	Martensitic + retained austenite	Peak aged	Z	3	–	0.1	847	Rafi et al. (2013b)
PH1	–	MMPDS	–	0.2	–	0.1	1120	
15–5 PH (H900)	Martensitic	Heat-treated 1 h at 482 °C in air	–	–	–	0.1	846	Wegener et al. (2013)
316L	Austenitic	As-built	–	10	–	0.1	165	(Spierings et al. 2011)
		Machined		0.4			210	
		Polished		0.1			268	
17–4 PH	Martensitic	As-built	XY	–	0.3	− 1 (rotating bending)	282[a,c]	Yadollahi et al. (2017)
			Z		0.26		202[a,c]	
		Heat-treated	XY		–		329 [a,c]	
			Z		–		181 [a,c]	
316L	–	As-built	–	13.29	–	− 1 (rotating bending)	130[a]	Uhlmann et al. (2017)
		Vibratory finished		1.74			170[a]	
		Turned		1.08			240[a]	
316L	–	As-built	–	–	–	− 1	108[a]	Riemer et al. (2014)
		Turned					267[a]	
		650 °C + Turned					294[a]	
		HIP + Turned					317[a]	
316L	–	As-built 1[b]	–	–	0.1	0.1	403[a]	(M. Zhang et al. 2018a)
		As-built 2[b]			0.1		400[a]	
		As-built 3[b]			1.15		395[a]	
		As-built 4[b]			6.56		148[a]	
		Annealed (982 °C for 25 min)			–		402	
		Annealed (1093 °C for 25 min)			–		40	
MARLOCK	–	As-built	XY	2.587	–	− 1	345[b]	(Miroslav et al. 2017)
		Machined		0.198			500[b]	

[a]At 10^6 cycles

[b]At 6×10^6 cycles

[c]S-N curve is plotted as σa vs 2 N

[d]As-built 1, 2, 3 and 4 are printed with layer thickness 20, 40, 60, 80 μm respectively

et al. 2015). Spierings et al. (2011) performed HCF test on 316L, however, the predicted fatigue strength limit as 172 MPa, which is lower than Reimer's experimental data (267 MPa), as shown in Table 8. Use of lower laser power by Spierings et al. (2011) could be a reason for low fatigue strength, as it causes higher defect formation and early failure. However, in both of the studies, L-PBF 316L alloy shows comparable fatigue strength with traditional casting (Strizak et al. 2005), as shown in Fig. 20. Unlike Al-alloy, defect formation and the associated change in fatigue life of 316L is not much sensitive with the change in layer thickness. Zhang et al. (2018a) showed no substantial change in fatigue life upon the change in layer

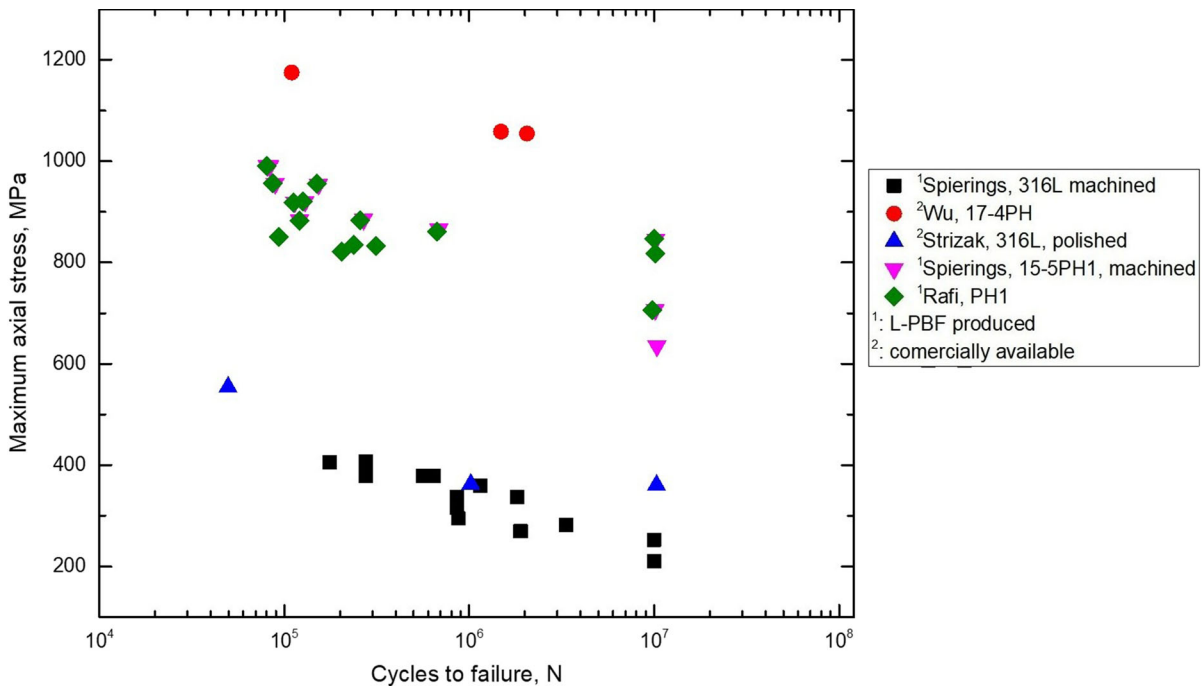

Fig. 20 Comparison of fatigue life of L-PBF produced steel parts with wrought steel parts at $R = 0.1$ (data from literature and re-plotted Rafi et al. 2013b; Spierings et al. 2011; Strizak et al. 2005; Wegener et al. 2013; Wu and Lin 2002))

thickness between 20 and 60 µm. Only a very higher layer thickness (80 µm) caused significant reduction in the part density as well as fatigue strength.

Fatigue behaviour of the steel is governed by defects and microstructure properties which can be tailored through various heat treatments. However, the sensitivity of the fatigue behaviour is not consistent with all types of heat treatment, and it can vary for HCF and LCF regimes as well. Stress relief treatment does not significantly improve overall fatigue life (crack initiation + propagation), although it delays crack initiation by removing internal residual stress (Afkhami et al. 2019). Fatigue crack initiation is mostly from grain boundary defects. Annealing changes grain size and removes significant defects on boundaries, thus shifts the fracture tendency from grain defects to pore defects remaining after annealing (Zhang et al. 2018b). This procedure provides a better fatigue life.

Heat treatment has been reported to improve the fatigue life of L-PBF 316L steel in the HCF regime and lower the fatigue life for LCF (Leuders et al. 2014; Zhang et al. 2018b). The reduction in LCF is coarsening grain size through the Hall Petch (Callister and Rethwisch 2012) effect as fatigue life of this alloy mainly depends on monotonic strength than pores (Leuders et al. 2014). At very high cycle regimes, internal pores cause crack initiation; therefore, heat treatment increases fatigue life by removing pores. The opposite behaviour has been found for 17-PH steel, where annealing is beneficial for LCF and unfavourable for HCF (Yadollahi et al. 2017). Heat treatment of 17-PH steel causes precipitation strengthening that leads to the formation of more defects as well as low HCF properties. However, this strengthening mechanism improves tensile and LCF properties (Leuders et al. 2014; Mahmoudi et al. 2017; Yadollahi et al. 2017). These findings reveal that both grain size and defects can affect the fatigue life of steel, in ways different to the other alloys. Therefore, the choice of heat treatment on steel fatigue must be application dependent. Like other AM alloys, the fatigue strength in steel is lower in the vertically built direction due to the formation of interlayer defects (Miroslav et al. 2017; Wegener et al. 2013; Yadollahi et al. 2017).

4.3.1 Crack growth properties of steel parts

FCG behaviour of L-PBF steels is similar to conventional processing, providing only a slight difference in

Table 9 FCG threshold value for L-PBF steel parts

Alloy types	Process condition	Orientation	Test type	Crack growth resistance (ΔK_{th})	References
316L	As-built	*CD* ⊥ *BD*	R = 0.1	4.3	Riemer et al. (2014)
		CD ∥ *BD*		3.0	
	Stress-relived (650 °C)	*CD* ⊥ *BD*		–	
		CD ∥ *BD*		4.0	
	HIP	*CD* ⊥ *BD*		4.6	
		CD ∥ *BD*		4.7	
316L	Single-melt (500 °C 1 h)	*CD* ⊥ *BD*	R = 0.1	9.9	Suryawanshi et al. (2017a)
		CD ∥ *BD*		9.1	
	Checkerboard (500 °C, 1 h)	*CD* ⊥ *BD*		8.1	
		CD ∥ *BD*		7.8	
				10–15 (Boyer 1985)	
18Ni (300)	Aging(@480 °C)	*CD* ⊥ *BD*	R = 0.1	5.8	Suryawanshi et al. (2017b)
				5.6	
	Wrought material	*CD* ∥ *BD*		5.3–5.7	

the threshold value. The literature data on crack growth threshold value for L-PBF steel are listed in Table 9. From this, a minor difference in the threshold value between horizontal and vertical built specimens is observed in the as-built and heat-treated conditions. This variation is because the columnar grains observed in L-PBF steel, oriented along the build direction provide a crack path along grain boundaries for horizontal samples, while the crack path is more tortuous in vertical samples (Riemer et al. 2014). Figure 21 shows a schematic representation to understand the crack growth anisotropy behaviour. However, HIP treatment introduces a bimodal grain structure (equiaxed and columnar), thus reducing the anisotropy of crack growth (Afkhami et al. 2019).

Although a significant benefit can be observed in yield strength of L-PBF 316L SS compared to conventional processes, a lack of strain hardening causes a decrease in elongation. This high yield strength is due to the extremely fine microstructure of L-PBF 316L steel, which causes stress-induced austenite to martensite transformation (SIMT). As expected, the above change in tensile properties results in a reduction in fracture toughness and threshold properties (Liu 2005). However, the HIP treatment that causes a decrease in porosity and recrystallization can improve the threshold value of 316L steel from 3.0 to 4.6 MPa $\sqrt{m}$ (Riemer et al. 2014), Table 9. In contrast, for 300 M steel (Liu et al. 2017), a lower fatigue threshold value and accelerated crack growth rate upon heating are noticed due to grain refinement that reduces the crack closure effects. This study also concluded that the stress ratio and stress level also decrease the crack growth threshold value.

Aging treatment on L-PBF produced 18Ni-300 steel (Suryawanshi et al. 2017b) improves fatigue behaviour by increasing crack growth threshold (Table 9), close to the value (5.5–5.7 MPa $\sqrt{m}$) of wrought material available in the literature for aged maraging steel (Bathias and Pelloux 1973). Herman et al. (Hermann Becker and Dimitrov 2016) studied the same alloy subjected to solution annealing and aging and found lower crack growth rate for the annealed condition. Besides, heat treatment reduces the anisotropy on FCG behaviour. An increase in the threshold value is observed for both HIP and stress relief treatment (Riemer et al. 2014; Suryawanshi et al. 2017a).

As seen in this section, most of the work pertaining to L-PBF produced steel is for 316L alloy. This alloy provides excellent tensile and fatigue properties, even in the as-built condition. Like Al-alloy, the effect of heat treatment on the fatigue life of steels is not very straightforward. Similar heat treatment causes

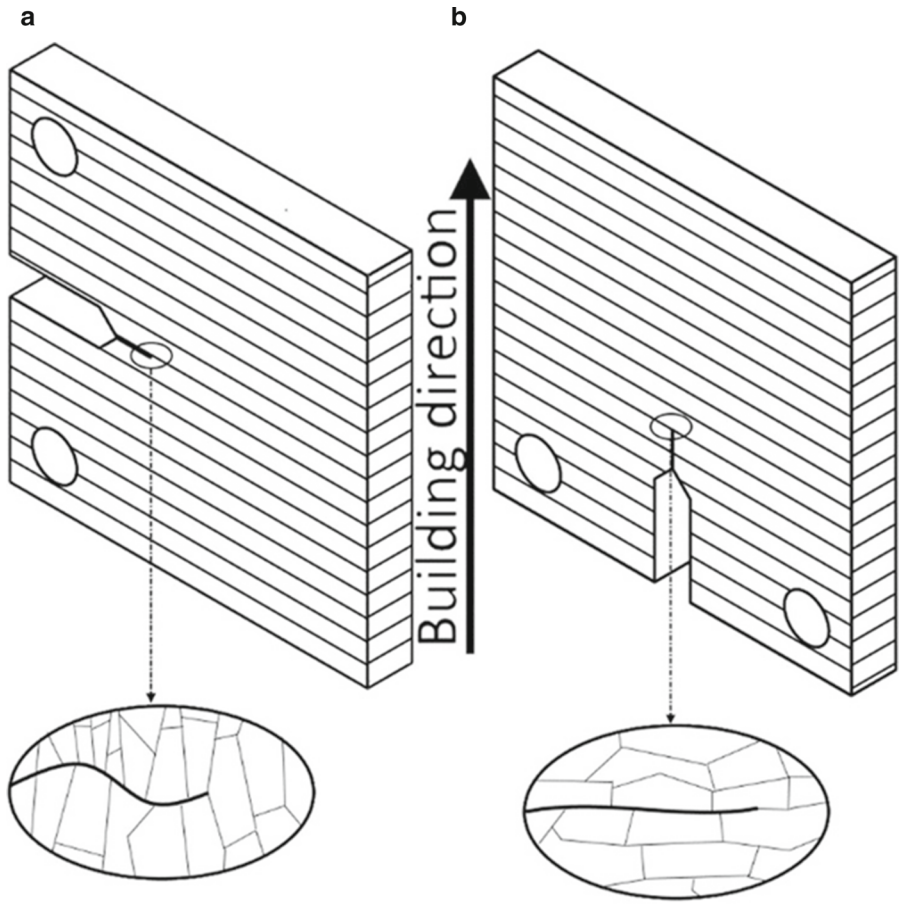

Fig. 21 Crack growth: **a** perpendicular, **b** parallel to build direction through microstructure in steel (Afkhami et al. 2019)

different microstructure formation among various steel type depending on alloy composition. Therefore, the choice of heat treatment needs to be customised for the particular type of steel and expected application requirements..

5 Summary and future outlook

Titanium, Aluminium and Steel are three common engineering alloys available for AM components which are often exposed to cyclic loading during operation.

In this article, an overview of the current state of these alloys is discussed focussing on fracture and fatigue behaviour. The following general features are found for all these alloys processed in L-PBF condition.

- As-built static tensile strength of AM fabricated parts is higher than that of wrought or cast parts because of the formation of a fine microstructure during the fast solidification rate; however, this results in a lower elongation.
- Fatigue strength, crack growth threshold and fracture toughness are very low for as-built AM samples compared to heat-treated samples.
- HCF behaviour is hierarchically controlled by surface roughness, micro-porosity and microstructure. The significant defects that are observed are gas pores and lack of fusion pores. However, the effect of LOF pores is more severe, depending on its location and orientation.
- For both static and fatigue loading conditions, anisotropy is observed for as-built samples. Vertical samples show the lowest mechanical performance. This is attributed grain size and defect location.
- Overall, the variation in the process parameter of the L-PBF process is the critical factor to control

defect formation, surface quality and microstructure evolution. Therefore, both static and fatigue strength may vary with the change in process parameters, such as layer thickness and laser power.

Besides, the effect of the various controlling factor on fatigue life can be summarised as in Table 10.

The salient features of this current study regarding fatigue properties are summarized in the following sections based on specific alloy types.

5.1 Titanium alloy

Majority of the published fatigue works are on Ti–6Al–4V alloy, producing valuable insights on the effects of microstructure, defects and post-processing that can be summarized as follows.

(a) Fatigue strength of as-built L-PBF Ti-alloy is higher than that produced by other AM processes as L-PBF yields higher part density (almost 99.99%).
(b) HIP treatment is the most effective for L-PBF Ti-alloys, which significantly increases the fatigue performance by reducing internal porosity. Nevertheless, HIP and polishing's combine effect provides the highest fatigue strength as improving both part density and surface quality.
(c) In addition to HIP, annealed and milled samples also show improved fatigue strength than as-built condition. However, this effect is not consistent.
(d) For Ti-Alloy, fine lamellar $\alpha + \beta$ microstructure shows higher crack growth resistance, thus providing an improved fatigue strength. Nevertheless, the effect of microstructure only becomes prominent at low porosity density.
(e) Similar to axial fatigue strength, the ΔK_{th} value for Ti-alloy is very low in the as-built condition, which increases by HIP or annealing.
(f) A few studies observed anisotropy in crack propagation behaviour, where the ΔK_{th} value parallel to the build direction is higher than perpendicular to it. Heat treatment removes this anisotropy while a slight difference is still notified in some literature.
(g) Almost all AM-processed Ti-alloy shows a minor variation of crack growth rate for annealed and HIP treated samples in the Paris region of the FCG curve.

Table 10 Effect of various controlling factors on fatigue strength

Controlling factors	Findings
Surface roughness	Fatigue failure initiates at the surface or subsurface defects
	Machining improves fatigue life
	Causes high scatter in the S–N curve
	Shows poor fatigue life irrespective of pore density
Porosity	Pores controls crack initiation
	Pore location > pore size > pore volume
	Heat treatment reduces porosity
Microstructure	Fine microstructure enhances crack propagation
Anisotropy	Horizontal build samples show higher fatigue strength than other build directions
	Heat treatment and platform heating reduce the anisotropy effect

5.2 Aluminium-alloy

From the available literature, the following observations can be made for Aluminium alloy.

(a) L-PBF Al-alloy exhibits early failure, and high scatter in S–N curve in the as-fabricated condition due to surface roughness and internal defects.
(b) Both base plate heating and T6 treatment in Al-alloy modify the microstructure by coarsening the dendrites, thus providing significant improvement in fatigue strength. However, few studies have shown adverse effects of prolonged heat treatment on fatigue life.
(c) In contrast to Ti-alloy, HIP or stress relief treatment does not appreciably improve the fatigue strength in Al-alloy, though it drastically reduces the internal porosity. Instead, machined and polished samples provide better fatigue performance than HIP; this implies that surface roughness is a critical factor for crack initiation in Al-alloys.

(d) Fatigue is influenced by surface treatment, which dominates at low-stress levels. In contrast, at high stress and very high cycle fatigue loading conditions, porosity has significant consequences, as cracks initiate from small internal pores.
(e) FCG threshold value is usually low for Al-alloy in as-built condition, and it increased after heat treatment. Heat treatment usually removes the anisotropy effect of axial fatigue strength in the S–N curve. In contrast, the FCG threshold value obtained from the notched test shows anisotropy even after heat treatment. Besides, for a notched sample, the growth rate of a crack parallel to the build direction is faster than the crack perpendicular to it. This crack growth behaviour of Al-alloy is opposite to that observed in Ti-alloy upon heat treatment.

5.3 Steel

According to the available research of L-PBF steels reviewed here:

(a) 316L steel exhibits comparatively high fatigue strength even in as-built condition as fewer defects are generated compared to other L-PBF steels. Fatigue strength of as-built 17-PH steel part is inferior compared to that obtained by traditional processing.
(b) The crack growth rate of L-PBF steels is higher for the cracks parallel to the build direction, compared to that perpendicular to it. This trend is similar to L-PBF Al-alloys.
(c) Post-processing heat treatment does not show similar change in the threshold value of L-PBF steels in all the build orientations. The crack growth rate in steel depends on grain size and location relative to the crack path. Therefore, in AM steels, the effect of heat treatment on fatigue life depends on the type of grain refinement, which varies with the type of steel.

5.4 Future scope

AM technique appeals to the aircraft and automotive industries, as it can save almost 30% (Frazier 2014) of the fuel costs compared to traditional fabrication by introducing intricate lightweight design and reducing assembly and machining operation. Reducing fuel cost implies less CO_2 footprint on this planet, which is the utmost goal for the research communities worldwide. Aircraft industries have already produced metal AM parts for the propulsion systems, including fuel injectors, gas generator duct, pogo z-baffle, turbo-pump inducer, chambers, and nozzles (Barroqueiro et al. 2019). These industries are planning to print more parts through 3D printing as well (Gorsse et al. 2017; Herzog et al. 2016; Yadollahi and Shamsaei 2017). This implies a clear need for increasing the reliability of printable AM materials by investigating FAIL-SAFE (Broek 1986) and damage-tolerant design (Griffith and Taylor 1921; Irwin 1958) properties, along with SAFE-LIFE properties, which will be implemented for future design of AM parts (Barter et al. 1993).

The current study has highlighted salient fatigue features of available AM alloys; therefore, it will help understand the potential effects of various factors, and use this knowledge to convey further extensive research.

Funding Open Access funding enabled and organized by CAUL and its Member Institutions. Funding was provided by RMIT University (RMIT Research Stipend Scholarship).

References

Aboulkhair NT, Tuck C, Ashcroft I, Maskery I, Everitt NM (2015) On the precipitation hardening of selective laser melted AlSi10Mg. Metall Mater Trans A 46(8):3337–3341. https://doi.org/10.1007/s11661-015-2980-7

Aboulkhair NT, Maskery I, Tuck C, Ashcroft I, Everitt NM (2016a) Improving the fatigue behaviour of a selectively laser melted aluminium alloy: Influence of heat treatment

and surface quality. Mater Des 104:174–182. https://doi.org/10.1016/j.matdes.2016.05.041

Aboulkhair NT, Maskery I, Tuck C, Ashcroft I, Everitt NM (2016b) The microstructure and mechanical properties of selectively laser melted AlSi10Mg: The effect of a conventional T6-like heat treatment. Mater Sci Eng 667:139–146. https://doi.org/10.1016/j.msea.2016.04.092

Aboulkhair NT, Simonelli M, Parry L, Ashcroft I, Tuck C, Hague R (2019) 3D printing of aluminium alloys: additive manufacturing of aluminium alloys using selective laser melting. Prog Mater Sci. https://doi.org/10.1016/j.pmatsci.2019.100578

Afkhami S, Dabiri M, Alavi SH, Björk T, Salminen A (2019) Fatigue characteristics of steels manufactured by selective laser melting. Int J Fatigue 122:72–83. https://doi.org/10.1016/j.ijfatigue.2018.12.029

Agius D, Kourousis KI, Wallbrink C, Song T (2017) Cyclic plasticity and microstructure of as-built SLM Ti–6Al–4V: the effect of build orientation. Mater Sci Eng, A 701:85–100. https://doi.org/10.1016/j.msea.2017.06.069

Agius D, Kourousis KI, Wallbrink C (2018) A review of the as-built SLM Ti–6Al–4V mechanical properties towards achieving fatigue resistant designs. Metals. https://doi.org/10.3390/met8010075

Ahn SH, Montero M, Odell D, Roundy S, Wright PK (2002) Anisotropic material properties of fused deposition modeling ABS. Rapid Prototyp J 8(4):248–257. https://doi.org/10.1108/13552540210441166

Ahsan MN, Bradley R, Pinkerton AJ (2011) Microcomputed tomography analysis of intralayer porosity generation in laser direct metal deposition and its causes. J Laser Appl. https://doi.org/10.2351/1.3582311

Alcisto J, Enriquez A, Garcia H, Hinkson S, Steelman T, Silverman E, Valdovino P, Gigerenzer H, Foyos J, Ogren J, Dorey J, Karg K, McDonald T, Es-Said OS (2011) Tensile properties and microstructures of laser-formed Ti–6Al–4V. J Mater Eng Perform 20(2):203–212. https://doi.org/10.1007/s11665-010-9670-9

Ali H, Ma L, Ghadbeigi H, Mumtaz K (2017) In-situ residual stress reduction, martensitic decomposition and mechanical properties enhancement through high temperature powder bed pre-heating of selective laser melted Ti6Al4V. Mater Sci Eng a 695:211–220. https://doi.org/10.1016/j.msea.2017.04.033

Ali H, Ghadbeigi H, Mumtaz K (2018) Effect of scanning strategies on residual stress and mechanical properties of Selective Laser Melted Ti6Al4V. Mater Sci Eng A 712:175–187. https://doi.org/10.1016/j.msea.2017.11.103

Anil S, Anand PS, Alghamdi H, Jansen JA (2011) Dental implant surface enhancement and osseointegration. Implant Dent. https://doi.org/10.5772/706

Appleyard D (2015) Powering up on powder technology. Met Powder Rep 70(6):285–289. https://doi.org/10.1016/j.mprp.2015.08.075

ASTM B85-03 (2003) Standard specification for aluminum-alloy die castings. ASTM Int. https://doi.org/10.1520/B0085-03

Attar H, Calin M, Zhang LC, Scudino S, Eckert J (2014) Manufacture by selective laser melting and mechanical behavior of commercially pure titanium. Mater Sci Eng A 593:170–177. https://doi.org/10.1016/j.msea.2013.11.038

Awd M, Tenkamp J, Hirtler M, Siddique S, Bambach M, Walther F (2017) Comparison of microstructure and mechanical properties of Scalmalloy ® produced by selective laser melting and laser metal deposition. Materials (Basel) 11(1):17. https://doi.org/10.3390/ma11010017

Bagheri A, Mahtabi MJ, Shamsaei N (2018) Fatigue behavior and cyclic deformation of additive manufactured NiTi. J Mater Process Technol 252:440–453. https://doi.org/10.1016/j.jmatprotec.2017.10.006

Bai JY, Fan CL, Lin SB, Yang CL, Dong BL (2017) Mechanical properties and fracture behaviors of GTA-additive manufactured 2219-Al after an especial heat treatment. J Mater Eng Perform 26(4):1808–1816. https://doi.org/10.1007/s11665-017-2627-5

Bajaj P, Hariharan A, Kini A, Kürnsteiner P, Raabe D, Jägle EA (2020) Steels in additive manufacturing: a review of their microstructure and properties. Mater Sci Eng A. https://doi.org/10.1016/j.msea.2019.138633

Banerjee D, Williams JC (2013) Perspectives on titanium science and technology. Acta Mater 61(3):844–879. https://doi.org/10.1016/j.actamat.2012.10.043

Banerjee R, Genc A, Hill D, Collins PC, Fraser HL (2005) Nanoscale TiB precipitates in laser deposited Ti-matrix composites. Scripta Mater 53(12):1433–1437. https://doi.org/10.1016/j.scriptamat.2005.08.014

Barroqueiro B, Andrade-Campos A, Valente RAE, Neto V (2019) Metal additive manufacturing cycle in aerospace industry: a comprehensive review. J Manuf Mater Process 3(3):52. https://doi.org/10.3390/jmmp3030052

Barter S, Clayton J, Clark G (1993) Aspects of fatigue affecting the design and maintenence of modern military aircraft. Int J Fatigue 15(4):325–332. https://doi.org/10.1016/0142-1123(93)90382-z

Bathias C, Pelloux RM (1973) Fatigue crack propagation in martensitic and austenitic steels [Article]. Metall Trans 4(5):1265–1273. https://doi.org/10.1007/BF02644521

Bauereiß A, Scharowsky T, Körner C (2014) Defect generation and propagation mechanism during additive manufacturing by selective beam melting. J Mater Process Technol 214(11):2522–2528. https://doi.org/10.1016/j.jmatprotec.2014.05.002

Beevers E, Brandão A, Gumpinger J, Gschweitl M, Seyfert C, Hofbauer P, Rohr T, Ghidini T (2018) Fatigue properties and material characteristics of additively manufactured AlSi10Mg - Effect of the contour parameter on the microstructure, density, residual stress, roughness and mechanical properties. Int J Fatigue 117:148–162. https://doi.org/10.1016/j.ijfatigue.2018.08.023

Benedetti M, Fontanari V, Bandini M, Zanini F, Carmignato S (2018) Low-and high-cycle fatigue resistance of Ti–6Al–4V ELI additively manufactured via selective laser melting: mean stress and defect sensitivity. Int J Fatigue 107:96–109. https://doi.org/10.1016/j.ijfatigue.2017.10.021

Beretta S, Romano S (2017) A comparison of fatigue strength sensitivity to defects for materials manufactured by AM or traditional processes. Int J Fatigue 94:178–191. https://doi.org/10.1016/j.ijfatigue.2016.06.020

Boyer HE (1985) Atlas of fatigue curves. ASM International, Novelty

Boyer RR (1996) An overview on the use of titanium in the aerospace industry. Mater Sci Eng 213(1–2):103–114. https://doi.org/10.1016/0921-5093(96)10233-1

Brandão AD, Gumpinger J, Gschweitl M, Seyfert C, Hofbauer P, Ghidini T (2017) Fatigue properties of additively manufactured AlSi10Mg—surface treatment effect. Procedia Struct Integr 7:58–66. https://doi.org/10.1016/j.prostr.2017.11.061

Brandl E, Heckenberger U, Holzinger V, Buchbinder D (2012) Additive manufactured AlSi10Mg samples using Selective Laser Melting (SLM): microstructure, high cycle fatigue, and fracture behavior. Mater Des 34:159–169. https://doi.org/10.1016/j.matdes.2011.07.067

Broek D (1986) Elementary engineering fracture mechanics. Kluwer Academic, Dordrecht

Buchbinder D, Schleifenbaum H, Heidrich S, Meiners W, Bültmann J (2011) High power selective laser melting (HP SLM) of aluminum parts. Phys Procedia 12:271–278. https://doi.org/10.1016/j.phpro.2011.03.035

Callister WD, Rethwisch DG (2012) Fundamentals of materials science and engineering: an integrated approach, 4th edn. Wiley, New York

Cao F, Ravi Chandran KS (2017) The role of crack origin size and early stage crack growth on high cycle fatigue of powder metallurgy Ti–6Al–4V alloy. Int J Fatigue 102:48–58. https://doi.org/10.1016/j.ijfatigue.2017.05.004

Cao F, Zhang TT, Ryder MA, Lados DA (2018) A review of the fatigue properties of additively manufactured Ti–6Al–4V. JOM (1989) 70(3):349–357. https://doi.org/10.1007/s11837-017-2728-5

Carter LN, Martin C, Withers PJ, Attallah MM (2014) The influence of the laser scan strategy on grain structure and cracking behaviour in SLM powder-bed fabricated nickel superalloy. J Alloys Compd 615:338–347. https://doi.org/10.1016/j.jallcom.2014.06.172

Carter LN, Essa K, Attallah MM (2015) Optimisation of selective laser melting for a high temperature Ni-superalloy. Rapid Prototyp J 21(4):423–432. https://doi.org/10.1108/Rpj-06-2013-0063

Chastand V, Quaegebeur P, Maia W, Charkaluk E (2018) Comparative study of fatigue properties of Ti–6Al–4V specimens built by electron beam melting (EBM) and selective laser melting (SLM). Mater Charact 143:76–81. https://doi.org/10.1016/j.matchar.2018.03.028

Chen LY, Huang JC, Lin CH, Pan CT, Chen SY, Yang TL, Lin DY, Lin HK, Jang JSC (2017) Anisotropic response of Ti–6Al–4V alloy fabricated by 3D printing selective laser melting. Mater Sci Eng 682:389–395. https://doi.org/10.1016/j.msea.2016.11.061

Concept Laser GmbH. https://www.ge.com/additive/who-we-are/concept-laser

Dallago M, Zanini F, Carmignato S, Pasini D, Benedetti M (2018) Effect of the geometrical defectiveness on the mechanical properties of SLM biomedical Ti6Al4V lattices. Procedia Struct Integr 13:161–167. https://doi.org/10.1016/j.prostr.2018.12.027

Damon J, Dietrich S, Vollert F, Gibmeier J, Schulze V (2018) Process dependent porosity and the influence of shot peening on porosity morphology regarding selective laser melted AlSi10Mg parts. Addit Manuf 20:77–89. https://doi.org/10.1016/j.addma.2018.01.001

Daniewicz SR, Shamsaei N (2017) An introduction to the fatigue and fracture behavior of additive manufactured parts. Int J Fatigue 94:167. https://doi.org/10.1016/j.ijfatigue.2016.07.007

Das S (2003) Physical aspects of process control in selective laser sintering of metals. Adv Eng Mater 5(10):701–711. https://doi.org/10.1002/adem.200310099

Dawes J, Bowerman R, Trepleton R (2015) Introduction to the additive manufacturing powder metallurgy supply chain. Johnson Matthey Technol Rev 59(3):243–256. https://doi.org/10.1595/205651315X688686

de Formanoir C, Michotte S, Rigo O, Germain L, Godet S (2016) Electron beam melted Ti–6Al–4V: microstructure, texture and mechanical behavior of the as-built and heat-treated material. Mater Sci Eng A 652:105–119. https://doi.org/10.1016/j.msea.2015.11.052

Edgar J, Tint S (2015) Additive manufacturing technologies: 3D printing, rapid prototyping, and direct digital manufacturing. Johnson Matthey Technol Rev 59(3):193–198. https://doi.org/10.1595/205651315X688406

Edwards P, Ramulu M (2014) Fatigue performance evaluation of selective laser melted Ti–6Al–4V. Mater Sci Eng A 598:327–337. https://doi.org/10.1016/j.msea.2014.01.041

Edwards P, O'Conner A, Ramulu M (2013) Electron beam additive manufacturing of titanium components: properties and performance. J Manuf Sci Eng Trans Asme 135(6):061016

EOS Electro Optical Systems GmbH. (21/04/2022). https://www.eos.info/en

Facchini L, Magalini E, Robotti P, Molinari A (2009) Microstructure and mechanical properties of Ti–6Al–4V produced by electron beam melting of pre-alloyed powders. Rapid Prototyp J 15(3):171–178. https://doi.org/10.1108/13552540910960262

Facchini L, Vicente N Jr, Lonardelli I, Magalini E, Robotti P, Molinari A (2010) Metastable austenite in 17–4 precipitation-hardening stainless steel produced by selective laser melting. Adv Eng Mater 12(3):184–188. https://doi.org/10.1002/adem.200900259

Fatemi A, Molaei R, Sharifimehr S, Shamsaei N, Phan N (2017) Torsional fatigue behavior of wrought and additive manufactured Ti-6A1-4V by powder bed fusion including surface finish effect. Int J Fatigue 99:187–201. https://doi.org/10.1016/j.ijfatigue.2017.03.002

Ferrar B, Mullen L, Jones E, Stamp R, Sutcliffe CJ (2012) Gas flow effects on selective laser melting (SLM) manufacturing performance. J Mater Process Technol 212(2):355–364. https://doi.org/10.1016/j.jmatprotec.2011.09.020

Fousova M, Dvorsky D, Michalcova A, Vojtech D (2018) Changes in the microstructure and mechanical properties of additively manufactured AlSi10Mg alloy after exposure to elevated temperatures. Mater Charact 137:119–126. https://doi.org/10.1016/j.matchar.2018.01.028

Fox JC, Moylan SP, Lane BM (2016) Effect of process parameters on the surface roughness of overhanging structures in laser powder bed fusion additive manufacturing. Procedia CIRP 45:131–134. https://doi.org/10.1016/j.procir.2016.02.347

Frazier WE (2014) Metal additive manufacturing: a review. J Mater Eng Perform 23(6):1917–1928. https://doi.org/10.1007/s11665-014-0958-z

Furuya Y, Takeuchi E (2014) Gigacycle fatigue properties of Ti–6Al–4V alloy under tensile mean stress. Mater Sci Eng 598:135–140. https://doi.org/10.1016/j.msea.2014.01.019

Galarraga H, Warren RJ, Lados DA, Dehoff RR, Kirka MM (2017) Fatigue crack growth mechanisms at the microstructure scale in as-fabricated and heat treated Ti–6Al–4V ELI manufactured by electron beam melting (EBM). Eng Fract Mech 176: 263–280. https://doi.org/10.1016/j.engfracmech.2017.03.024

Godec M, Zaefferer S, Podgornik B, Šinko M, Tchernychova E (2020) Quantitative multiscale correlative microstructure analysis of additive manufacturing of stainless steel 316L processed by selective laser melting. Mater Charact 160: 110074. https://doi.org/10.1016/j.matchar.2019.110074

Gong H, Rafi K, Gu H, Starr T, Stucker B (2014a) Analysis of defect generation in Ti–6Al–4V parts made using powder bed fusion additive manufacturing processes. Addit Manuf 1–4:87–98. https://doi.org/10.1016/j.addma.2014.08.002

Gong X, Anderson T, Chou K (2014b) Review on powder-based electron beam additive manufacturing technology. Manuf Rev (Ulis, France) 1:2. https://doi.org/10.1051/mfreview/2014001

Gong H, Rafi K, Gu H, Janaki Ram GD, Starr T, Stucker B (2015) Influence of defects on mechanical properties of Ti–6Al–4V components produced by selective laser melting and electron beam melting. Mater Des 86:545–554. https://doi.org/10.1016/j.matdes.2015.07.147

Gorsse S, Hutchinson C, Goune M, Banerjee R (2017) Additive manufacturing of metals: a brief review of the characteristic microstructures and properties of steels, Ti–6Al–4V and high-entropy alloys. Sci Technol Adv Mater 18(1):584–610. https://doi.org/10.1080/14686996.2017.1361305

Gorynin IV (1999) Titanium alloys for marine application. Mater Sci Eng 263(2):112–116. https://doi.org/10.1016/S0921-5093(98)01180-0

Greitemeier D, Dalle Donne C, Syassen F, Eufinger J, Melz T (2016) Effect of surface roughness on fatigue performance of additive manufactured Ti–6Al–4V. Mater Sci Technol 32(7):629–634. https://doi.org/10.1179/1743284715y.0000000053

Greitemeier D, Palm F, Syassen F, Melz T (2017) Fatigue performance of additive manufactured TiAl6V4 using electron and laser beam melting. Int J Fatigue 94:211–217. https://doi.org/10.1016/j.ijfatigue.2016.05.001

Griffith AA, Taylor GI (1921) VI The phenomena of rupture and flow in solids. Philos Trans R Soc Lond Ser A 221(582–593):163–198. https://doi.org/10.1098/rsta.1921.0006

Gu D (2015) Laser additive manufacturing of high-performance materials, 1st edn. Springer, Berlin/Heidelberg. https://doi.org/10.1007/978-3-662-46089-4

Gu D, Shen Y (2009) Balling phenomena in direct laser sintering of stainless steel powder: Metallurgical mechanisms and control methods. Mater Des 30(8):2903–2910. https://doi.org/10.1016/j.matdes.2009.01.013

Gu H, Gong H, Pal D, Rafi K, Starr T, Stucker B (2013) Influences of energy density on porosity and microstructure of selective laser melted 17-4PH stainless steel. In: 2013 Solid Freeform Fabrication Symposium

Günther J, Krewerth D, Lippmann T, Leuders S, Tröster T, Weidner A, Biermann H, Niendorf T (2017) Fatigue life of additively manufactured Ti–6Al–4V in the very high cycle fatigue regime. Int J Fatigue 94:236–245. https://doi.org/10.1016/j.ijfatigue.2016.05.018

Gurrappa I (2003) Characterization of titanium alloy Ti–6Al–4V for chemical, marine and industrial applications. Mater Charact 51(2–3):131–139. https://doi.org/10.1016/j.matchar.2003.10.006

Hann DB, Iammi J, Folkes J (2011) A simple methodology for predicting laser-weld properties from material and laser parameters. J Phys D. https://doi.org/10.1088/0022-3727/44/44/445401

Hao Y-L, Li S-J, Yang R (2016) Biomedical titanium alloys and their additive manufacturing. Rare Met 35(9):661–671. https://doi.org/10.1007/s12598-016-0793-5

Herderick E (2011) Additive manufacturing of metals: A review. In: Materials Science & Technology 2011 Conference and Exhibition (MS&T Partner Societies)

Hermann Becker T, Dimitrov D (2016) The achievable mechanical properties of SLM produced Maraging Steel 300 components. Rapid Prototyp J 22(3):487–494. https://doi.org/10.1108/RPJ-08-2014-0096

Herzog D, Seyda V, Wycisk E, Emmelmann C (2016) Additive manufacturing of metals. Acta Mater 117:371–392. https://doi.org/10.1016/j.actamat.2016.07.019

Holmes J, Queeney RA (1985) Fatigue crack initiation in a porous steel. Powder Metall 28(4):231–235. https://doi.org/10.1179/pom.1985.28.4.231

Irwin GR (1958) Fracture. In: Flügge S (ed) Elasticity and Plasticity [Elastizität und Plastizität]. Springer, Berlin/Heidelberg, pp 551–590. https://doi.org/10.1007/978-3-642-45887-3_5

Islam M, Purtonen T, Piili H, Salminen A, Nyrhilä O (2013) Temperature profile and imaging analysis of laser additive manufacturing of stainless steel. Phys Procedia 41:835–842. https://doi.org/10.1016/j.phpro.2013.03.156

Jägle EA, Choi P-P, Van Humbeeck J, Raabe D (2014) Precipitation and austenite reversion behavior of a maraging steel produced by selective laser melting. J Mater Res 29(17):2072–2079. https://doi.org/10.1557/jmr.2014.204

Kang N, El Mansori M, Guittonneau F, Liao H, Fu Y, Aubry E (2018) Controllable mesostructure, magnetic properties of soft magnetic Fe-Ni-Si by using selective laser melting from nickel coated high silicon steel powder. Appl Surf Sci 455:736–741. https://doi.org/10.1016/j.apsusc.2018.06.045

Kasperovich G, Hausmann J (2015) Improvement of fatigue resistance and ductility of TiAl6V4 processed by selective laser melting. J Mater Process Technol 220:202–214. https://doi.org/10.1016/j.jmatprotec.2015.01.025

Kempen K, Yasa E, Thijs L, Kruth JP, Van Humbeeck J (2011) Microstructure and mechanical properties of selective laser melted 18Ni-300 steel. Phys Procedia 12:255–263. https://doi.org/10.1016/j.phpro.2011.03.033

Kempen K, Vrancken B, Buls S, Thijs L, Van Humbeeck J, Kruth J-P (2014) Selective laser melting of crack-free high density M2 high speed steel parts by baseplate preheating. J Manuf Sci Eng. https://doi.org/10.1115/1.4028513

Kempen K, Thijs L, Vrancken B, Buls S, Humbeeck J, Kruth J-P (2013) Producing crack-free, high density M2 HSS parts by selective laser melting: pre-heating the baseplate. In: 24th International SFF Symposium—An Additive Manufacturing Conference 13

Khairallah SA, Anderson AT, Rubenchik A, King WE (2016) Laser powder-bed fusion additive manufacturing: physics of complex melt flow and formation mechanisms of pores, spatter, and denudation zones. Acta Mater 108:36–45. https://doi.org/10.1016/j.actamat.2016.02.014

Kimura T, Nakamoto T (2016) Microstructures and mechanical properties of A356 (AlSi7Mg0. 3) aluminum alloy fabricated by selective laser melting. Mater Des 89:1294–1301. https://doi.org/10.1016/j.matdes.2015.10.065

King WE, Barth HD, Castillo VM, Gallegos GF, Gibbs JW, Hahn DE, Kamath C, Rubenchik AM (2014) Observation of keyhole-mode laser melting in laser powder-bed fusion additive manufacturing. J Mater Process Technol 214(12):2915–2925. https://doi.org/10.1016/j.jmatprotec.2014.06.005

Kodama H (1981) Automatic method for fabricating a three-dimensional plastic model with photo-hardening polymer. Rev Sci Instrum 52(11):1770–1773. https://doi.org/10.1063/1.1136492

Kong DC, Ni XQ, Dong CF, Zhang L, Man C, Cheng XQ, Li XG (2019) Anisotropy in the microstructure and mechanical property for the bulk and porous 316L stainless steel fabricated via selective laser melting. Mater Lett 235:1–5. https://doi.org/10.1016/j.matlet.2018.09.152

Koutiri I, Pessard E, Peyre P, Amlou O, De Terris T (2018) Influence of SLM process parameters on the surface finish, porosity rate and fatigue behavior of as-built Inconel 625 parts. J Mater Process Technol 255:536–546. https://doi.org/10.1016/j.jmatprotec.2017.12.043

Kruth J, P, Mercelis, Van Vaerenbergh J, Froyen L, Rombouts M (2005) Binding mechanisms in selective laser sintering and selective laser melting. Rapid Prototyp J 11(1):26–36. https://doi.org/10.1108/13552540510573365

Kruth J-P, Deckers J, Yasa E, Wauthlé R (2012) Assessing and comparing influencing factors of residual stresses in selective laser melting using a novel analysis method. Proc Inst Mech Eng B 226(6):980–991. https://doi.org/10.1177/0954405412437085

Lados DA, Apelian D (2004) Fatigue crack growth characteristics in cast Al–Si–Mg alloys: Part I. Effect of processing conditions and microstructure. Mater Sci Eng 385(1):200–211. https://doi.org/10.1016/j.msea.2004.06.073

Larrosa NO, Wang W, Read N, Loretto MH, Evans C, Carr J, Tradowsky U, Attallah MM, Withers PJ (2018) Linking microstructure and processing defects to mechanical properties of selectively laser melted AlSi10Mg alloy. Theoret Appl Fract Mech 98:123–133. https://doi.org/10.1016/j.tafmec.2018.09.011

Leary M, Mazur M, Williams H, Yang E, Alghamdi A, Lozanovski B, Zhang XZ, Shidid D, Farahbod-Sternahl L, Witt G, Kelbassa I, Choong P, Qian M, Brandt M (2018) Inconel 625 lattice structures manufactured by selective laser melting (SLM): mechanical properties, deformation and failure modes. Mater Des 157:179–199. https://doi.org/10.1016/j.matdes.2018.06.010

LeBrun T, Nakamoto T, Horikawa K, Kobayashi H (2015) Effect of retained austenite on subsequent thermal processing and resultant mechanical properties of selective laser melted 17–4 PH stainless steel. Mater Des 81:44–53. https://doi.org/10.1016/j.matdes.2015.05.026

Lee YS, Farson DF (2016) Surface tension-powered build dimension control in laser additive manufacturing process. Int J Adv Manuf Technol 85(5):1035–1044. https://doi.org/10.1007/s00170-015-7974-5

Leuders S, Thöne M, Riemer A, Niendorf T, Tröster T, Richard H, Maier H (2013) On the mechanical behaviour of titanium alloy TiAl6V4 manufactured by selective laser melting: Fatigue resistance and crack growth performance. Int J Fatigue 48:300–307. https://doi.org/10.1016/j.ijfatigue.2012.11.011

Leuders S, Lieneke T, Lammers S, Tröster T, Niendorf T (2014) On the fatigue properties of metals manufactured by selective laser melting—the role of ductility. J Mater Res 29(17):1911–1919. https://doi.org/10.1557/jmr.2014.157

Lewandowski JJ, Seifi M (2016) Metal additive manufacturing: a review of mechanical properties. Annu Rev Mater Res 46(1):151–186. https://doi.org/10.1146/annurev-matsci-070115-032024(AnnualReviewofMaterialsResearch)

Li R, Shi Y, Wang L, Liu J, Wang Z (2011) The key metallurgical features of selective laser melting of stainless steel powder for building metallic part. Powder Metall Met Ceram 50(3):141. https://doi.org/10.1007/s11106-011-9311-3

Li R, Liu J, Shi Y, Wang L, Jiang W (2012) Balling behavior of stainless steel and nickel powder during selective laser melting process. Int J Adv Manuf Technol 59(9):1025–1035. https://doi.org/10.1007/s00170-011-3566-1

Li PH, Guo WG, Yuan KB, Su Y, Wang JJ, Lin X, Li YP (2018) Effects of processing defects on the dynamic tensile mechanical behavior of laser-solid-formed Ti-6Al-4 V. Mater Charact 140:15–29. https://doi.org/10.1016/j.matchar.2018.03.032

Liu AF (2005) Mechanics and mechanisms of fracture: an introduction. ASM Int. https://doi.org/10.5860/choice.43-5914

Liu S, Shin YC (2019) Additive manufacturing of Ti6Al4V alloy: a review. Mater Des. https://doi.org/10.1016/j.matdes.2018.107552

Liu QC, Elambasseril J, Sun SJ, Leary M, Brandt M, Sharp PK (2014) The effect of manufacturing defects on the fatigue behaviour of Ti–6Al–4V specimens fabricated using selective laser melting. Adv Mater Res. https://doi.org/10.4028/www.scientific.net/AMR.891-892.1519

Liu F, Lin X, Yang H, Wen X, Li Q, Liu F, Huang W (2017) Effect of microstructure on the fatigue crack growth behavior of laser solid formed 300M steel. Mater Sci Eng A 695:258–264. https://doi.org/10.1016/j.msea.2017.04.001

Liu X, Zhao C, Zhou X, Shen Z, Liu W (2019) Microstructure of selective laser melted AlSi10Mg alloy. Mater Des. https://doi.org/10.1016/j.matdes.2019.107677

Liu B, Wildman R, Tuck C, Ashcroft I, Hague R (2011) Investigation the effect of particle size distribution on processing parameters optimisation in selective laser melting process. https://doi.org/10.26153/tsw/15290

Louvis E, Fox P, Sutcliffe CJ (2011) Selective laser melting of aluminium components. J Mater Process Technol 211(2):275–284. https://doi.org/10.1016/j.jmatprotec.2010.09.019

Lucas JJ, Konieczny PP (1971) Relationship between alpha grain size and crack initiation fatigue strength in Ti–6Al–

4V. Metall Trans 2(3):911–912. https://doi.org/10.1007/BF02662756

Lütjering G (1998) Influence of processing on microstructure and mechanical properties of (α+β) titanium alloys. Mater Sci Eng A 243(1):32–45. https://doi.org/10.1016/S0921-5093(97)00778-8

Mahmoudi M, Elwany A, Yadollahi A, Thompson SM, Bian LK, Shamsaei N (2017) Mechanical properties and microstructural characterization of selective laser melted 17–4 PH stainless steel. Rapid Prototyp J 23(2):280–294. https://doi.org/10.1108/rpj-12-2015-0192

Mall S, Namjoshi SA, Porter WJ (2004) Effects of microstructure on fretting fatigue crack initiation behavior of Ti–6Al–4V. Mater Sci Eng 383(2):334–340. https://doi.org/10.1016/j.msea.2004.05.019

Maskery I, Aremu AO, Simonelli M, Tuck C, Wildman RD, Ashcroft IA, Hague RJM (2015b) Mechanical properties of Ti–6Al–4V selectively laser melted parts with body-centred-cubic lattices of varying cell size. Exp Mech 55(7):1261–1272. https://doi.org/10.1007/s11340-015-0021-5

Maskery I, Aboulkhair NT, Aremu AO, Tuck CJ, Ashcroft IA, Wildman RD, Hague RJM (2016a) A mechanical property evaluation of graded density Al-Si10-Mg lattice structures manufactured by selective laser melting. Mater Sci Eng A 670:264–274. https://doi.org/10.1016/j.msea.2016.06.013

Maskery I, Aboulkhair NT, Corfield MR, Tuck C, Clare AT, Leach RK, Wildman RD, Ashcroft IA, Hague RJM (2016b) Quantification and characterisation of porosity in selectively laser melted Al–Si10–Mg using X-ray computed tomography. Mater Charact 111:193–204. https://doi.org/10.1016/j.matchar.2015.12.001

Maskery I, Aboulkhair NT, Tuck C, Wildman RD, Ashcroft IA, Everitt NM, Hague RJM (2015a) Fatigue performance enhancement of selectively laser melted aluminium alloy by heat treatment. In: 26th Annual International Solid Freeform Fabrication Symposium, Austin, Texas, USA

Masuo H, Tanaka Y, Morokoshi S, Yagura H, Uchida T, Yamamoto Y, Murakami Y (2018) Influence of defects, surface roughness and HIP on the fatigue strength of Ti–6Al–4V manufactured by additive manufacturing. Int J Fatigue 117:163–179. https://doi.org/10.1016/j.ijfatigue.2018.07.020

Meier H, Haberland C (2008) Experimental studies on selective laser melting of metallic parts. Materialwiss Werkstofftech 39(9):665–670. https://doi.org/10.1002/mawe.200800327

Melz T, Schoberth A, Jürgens M, Greitemeier D, Dalle Donne C, Eufinger J (2015) Uncertainty of additive manufactured Ti–6Al–4V: chemistry, microstructure and mechanical properties. Appl Mech Mater 807:169–180. https://doi.org/10.4028/www.scientific.net/AMM.807.169

Miroslav P, PavlÍna T, Jana H, Pavel Š, Boivie K (2017) A study of selective laser melting technology on the ultra-high strength tool steel use—quality, mechanical properties and fatigue. Springer, New York. https://doi.org/10.1007/978-3-319-41468-3_6

Mower TM, Long MJ (2016) Mechanical behavior of additive manufactured, powder-bed laser-fused materials. Mater Sci Eng 651:198–213. https://doi.org/10.1016/j.msea.2015.10.068

Murakami Y (2002) Metal Fatigue: Effects of Small Defects and Nonmetallic Inclusions Elsevier, Oxford. https://www.elsevier.com/books/metal-fatigue-effects-of-small-defects-and-nonmetallic-inclusions/murakami/978-0-12-813876-2

Murr LE, Gaytan SM, Ceylan A, Martinez E, Martinez JL, Hernandez DH, Machado BI, Ramirez DA, Medina F, Collins S, Wicker RB (2010) Characterization of titanium aluminide alloy components fabricated by additive manufacturing using electron beam melting. Acta Mater 58(5):1887–1894. https://doi.org/10.1016/j.actamat.2009.11.032

Murr LE, Gaytan SM, Ramirez DA, Martinez E, Hernandez J, Amato KN, Shindo PW, Medina FR, Wicker RB (2012a) Metal fabrication by additive manufacturing using laser and electron beam melting technologies. J Mater Sci Technol 28(1):1–14. https://doi.org/10.1016/S1005-0302(12)60016-4

Murr LE, Martinez E, Hernandez J, Collins S, Amato KN, Gaytan SM, Shindo PW (2012b) Microstructures and properties of 17–4 PH stainless steel fabricated by selective laser melting. J Market Res 1(3):167–177. https://doi.org/10.1016/S2238-7854(12)70029-7

Neikter M, Huang A, Wu X (2019) Microstructural characterization of binary microstructure pattern in selective laser-melted Ti–6Al–4V. Int J Adv Manuf Technol 104(1):1381–1391. https://doi.org/10.1007/s00170-019-04002-8

Ng GKL, Jarfors AEW, Bi G, Zheng HY (2009) Porosity formation and gas bubble retention in laser metal deposition. Appl Phys a-Mater Sci Process 97(3):641–649. https://doi.org/10.1007/s00339-009-5266-3

Olakanmi EO (2013) Selective laser sintering/melting (SLS/SLM) of pure Al, Al–Mg, and Al–Si powders: effect of processing conditions and powder properties. J Mater Process Technol 213(8):1387–1405. https://doi.org/10.1016/j.jmatprotec.2013.03.009

Palanivel S, Dutt AK, Faierson EJ, Mishra RS (2016) Spatially dependent properties in a laser additive manufactured Ti–6Al–4V component. Mater Sci Eng 654:39–52. https://doi.org/10.1016/j.msea.2015.12.021

Prashanth KG, Scudino S, Klauss HJ, Surreddi KB, Lober L, Wang Z, Chaubey AK, Kuhn U, Eckert J (2014a) Microstructure and mechanical properties of Al–12Si produced by selective laser melting: effect of heat treatment. Mater Sci Eng 590:153–160. https://doi.org/10.1016/j.msea.2013.10.023

Prashanth KG, Scudino S, Klauss HJ, Surreddi KB, Löber L, Wang Z, Chaubey AK, Kühn U, Eckert J (2014b) Microstructure and mechanical properties of Al–12Si produced by selective laser melting: effect of heat treatment. Mater Sci Eng A 590:153–160. https://doi.org/10.1016/j.msea.2013.10.023

Qian M, Xu W, Brandt M, Tang HP (2016) Additive manufacturing and postprocessing of Ti–6Al–4V for superior mechanical properties. MRS Bull 41(10):775–784. https://doi.org/10.1557/mrs.2016.215

Qiu C, Adkins NJ, Attallah MM (2013) Microstructure and tensile properties of selectively laser-melted and of HIPed laser-melted Ti–6Al–4V. Mater Sci Eng 578:230–239. https://doi.org/10.1016/j.msea.2013.04.099

Rafi HK, Karthik NV, Gong HJ, Starr TL, Stucker BE (2013a) Microstructures and mechanical properties of Ti6Al4V parts fabricated by selective laser melting and electron beam melting. J Mater Eng Perform 22(12):3872–3883. https://doi.org/10.1007/s11665-013-0658-0

Rafi HK, Starr TL, Stucker BE (2013b) A comparison of the tensile, fatigue, and fracture behavior of Ti–6Al–4V and 15–5 PH stainless steel parts made by selective laser melting. Int J Adv Manuf Technol 69(5):1299–1309. https://doi.org/10.1007/s00170-013-5106-7

Rai R, Elmer JW, Palmer TA, DebRoy T (2007) Heat transfer and fluid flow during keyhole mode laser welding of tantalum, Ti–6Al–4V, 304L stainless steel and vanadium. J Phys D-Appl Phys 40(18):5753–5766. https://doi.org/10.1088/0022-3727/40/18/037

Read N, Wang W, Essa K, Attallah MM (2015) Selective laser melting of AlSi10Mg alloy: process optimisation and mechanical properties development. Mater Des 65:417–424. https://doi.org/10.1016/j.matdes.2014.09.044

Riemer A, Leuders S, Thöne M, Richard HA, Tröster T, Niendorf T (2014) On the fatigue crack growth behavior in 316L stainless steel manufactured by selective laser melting. Eng Fract Mech 120:15–25. https://doi.org/10.1016/j.engfracmech.2014.03.008

Riemer A, Richard HA, Bruggemann JP, Wesendahl JN, DMRC (2015) Fatigue crack growth in additive manufactured products. Frattura Ed Integrita Strutturale 34:437–446. https://doi.org/10.3221/igf-esis.34.49

Romano S, Bruckner-Foit A, Brandao A, Gumpinger J, Ghidini T, Beretta S (2018) Fatigue properties of AlSi10Mg obtained by additive manufacturing: defect-based modelling and prediction of fatigue strength. Eng Fract Mech 187:165–189. https://doi.org/10.1016/j.engfracmech.2017.11.002

Saboori A, Gallo D, Biamino S, Fino P, Lombardi M (2017) An overview of additive manufacturing of titanium components by directed energy deposition: microstructure and mechanical properties. Appl Sci-Basel. https://doi.org/10.3390/app7090883

Sachs E, Cima M, Cornie J (1990) Three-dimensional printing: rapid tooling and prototypes directly from a CAD model. CIRP Ann 39(1):201–204. https://doi.org/10.1016/S0007-8506(07)61035-X

Sercombe TB, Li X (2016) Selective laser melting of aluminium and aluminium metal matrix composites: review. Mater Technol 31(2):77–85. https://doi.org/10.1179/1753555715Y.0000000078

Shamsaei N, Yadollahi A, Bian L, Thompson SM (2015) An overview of direct laser deposition for additive manufacturing; Part II: Mechanical behavior, process parameter optimization and control. Addit Manuf 8:12–35. https://doi.org/10.1016/j.addma.2015.07.002

Shifeng W, Shuai L, Qingsong W, Yan C, Sheng Z, Yusheng S (2014) Effect of molten pool boundaries on the mechanical properties of selective laser melting parts. J Mater Process Technol 214(11):2660–2667. https://doi.org/10.1016/j.jmatprotec.2014.06.002

Shrestha S, Starr T, Chou K (2019) A study of keyhole porosity in selective laser melting: single-track scanning with micro-CT analysis. J Manuf Sci Eng. https://doi.org/10.1115/1.4043622

Siddique S, Imran M, Rauer M, Kaloudis M, Wycisk E, Emmelmann C, Walther F (2015) Computed tomography for characterization of fatigue performance of selective laser melted parts. Mater Des 83:661–669. https://doi.org/10.1016/j.matdes.2015.06.063

Siddique S, Imran M, Walther F (2017) Very high cycle fatigue and fatigue crack propagation behavior of selective laser melted AlSi12 alloy. Int J Fatigue 94:246–254. https://doi.org/10.1016/j.ijfatigue.2016.06.003

Simonelli M, Tse YY, Tuck C (2014) Effect of the build orientation on the mechanical properties and fracture modes of SLM Ti–6Al–4V. Mater Sci Eng A 616:1–11. https://doi.org/10.1016/j.msea.2014.07.086

SLM Solutions GmbH. https://www.slm-solutions.com/

Sola A, Nouri A (2019) Microstructural porosity in additive manufacturing: the formation and detection of pores in metal parts fabricated by powder bed fusion. J Adv Manuf Process. https://doi.org/10.1002/amp2.10021

Spierings AB, Herres N, Levy G (2011) Influence of the particle size distribution on surface quality and mechanical properties in AM steel parts. Rapid Prototyp J 17(3):195–202. https://doi.org/10.1108/13552541111124770

Stephens RI, Fatemi A, Stephens RR, Fuchs HO (2000) Metal fatigue in engineering. Wiley. https://www.wiley.com/en-us/Metal+Fatigue+in+Engineering,+2nd+Edition-p-9780471510598

Sterling AJ, Torries B, Shamsaei N, Thompson SM, Seely DW (2016) Fatigue behavior and failure mechanisms of direct laser deposited Ti–6Al–4V. Mater Sci Eng A 655:100–112. https://doi.org/10.1016/j.msea.2015.12.026

Strizak JP, Tian H, Liaw PK, Mansur LK (2005) Fatigue properties of type 316LN stainless steel in air and mercury. J Nucl Mater 343(1–3):134–144. https://doi.org/10.1016/j.jnucmat.2005.03.019

Sun G, Zhou R, Lu J, Mazumder J (2015) Evaluation of defect density, microstructure, residual stress, elastic modulus, hardness and strength of laser-deposited AISI 4340 steel. Acta Mater 84:172–189. https://doi.org/10.1016/j.actamat.2014.09.028

Sun YY, Lu SL, Gulizia S, Oh CH, Fraser D, Leary M, Qian M (2020) Fatigue performance of additively manufactured Ti–6Al–4V: surface condition vs internal defects. Jom 72(3):1022–1030. https://doi.org/10.1007/s11837-020-04025-7

Suresh S (1998) Fatigue of materials. Cambridge University Press, Cambridge. https://doi.org/10.1017/CBO9780511806575

Suryawanshi J, Prashanth KG, Scudino S, Eckert J, Prakash O, Ramamurty U (2016) Simultaneous enhancements of strength and toughness in an Al-12Si alloy synthesized using selective laser melting. Acta Mater 115:285–294. https://doi.org/10.1016/j.actamat.2016.06.009

Suryawanshi J, Prashanth KG, Ramamurty U (2017a) Mechanical behavior of selective laser melted 316L stainless steel. Mater Sci Eng A 696:113–121. https://doi.org/10.1016/j.msea.2017.04.058

Suryawanshi J, Prashanth KG, Ramamurty U (2017b) Tensile, fracture, and fatigue crack growth properties of a 3D printed managing steel through selective laser melting. J Alloys Compd 725:355–364. https://doi.org/10.1016/j.jallcom.2017.07.177

Takata N, Kodaira H, Sekizawa K, Suzuki A, Kobashi M (2017) Change in microstructure of selectively laser melted AlSi10Mg alloy with heat treatments. Mater Sci Eng 704:218–228. https://doi.org/10.1016/j.msea.2017.08.029

Tammas-Williams S, Withers PJ, Todd I, Prangnell PB (2017) The influence of porosity on fatigue crack initiation in additively manufactured titanium components. Sci Rep. https://doi.org/10.1038/s41598-017-06504-5

Tan X, Kok Y, Tan YJ, Descoins M, Mangelinck D, Tor SB, Leong KF, Chua CK (2015) Graded microstructure and mechanical properties of additive manufactured Ti–6Al–4V via electron beam melting. Acta Mater 97:1–16. https://doi.org/10.1016/j.actamat.2015.06.036

Tang M, Pistorius PC (2017) Oxides, porosity and fatigue performance of AlSi10Mg parts produced by selective laser melting. Int J Fatigue 94:192–201. https://doi.org/10.1016/j.ijfatigue.2016.06.002

Thijs L, Verhaeghe F, Craeghs T, Humbeeck JV, Kruth J-P (2010) A study of the microstructural evolution during selective laser melting of Ti–6Al–4V. Acta Mater 58(9):3303–3312. https://doi.org/10.1016/j.actamat.2010.02.004

Thijs L, Kempen K, Kruth J-P, Van Humbeeck J (2013) Fine-structured aluminium products with controllable texture by selective laser melting of pre-alloyed AlSi10Mg powder. Acta Mater 61(5):1809–1819. https://doi.org/10.1016/j.actamat.2012.11.052

Tong J, Bowen CR, Persson J, Plummer A (2017) Mechanical properties of titanium-based Ti–6Al–4V alloys manufactured by powder bed additive manufacture. Mater Sci Technol 33(2):138–148. https://doi.org/10.1080/02670836.2016.1172787

Trevisan F, Calignano F, Lorusso M, Pakkanen J, Aversa A, Ambrosio EP, Lombardi M, Fino P, Manfredi D (2017) On the selective laser melting (SLM) of the AlSi10Mg alloy: process, microstructure, and mechanical properties. Materials. https://doi.org/10.3390/ma10010076

Trumpf GmbH. https://www.trumpf.com/en_INT/

Uhlmann E, Fleck C, Gerlitzky G, Faltin F (2017) Dynamical fatigue behavior of additive manufactured products for a fundamental life cycle approach. Procedia CIRP 61:588–593. https://doi.org/10.1016/j.procir.2016.11.138

Uzan NE, Shneck R, Yeheskel O, Frage N (2017) Fatigue of AlSi10Mg specimens fabricated by additive manufacturing selective laser melting (AM-SLM). Mater Sci Eng 704:229–237. https://doi.org/10.1016/j.msea.2017.08.027

Van der Schueren B, Kruth JP (1995) Powder deposition in selective metal powder sintering. Rapid Prototyp J 1(3):23–31. https://doi.org/10.1108/13552549510094241

Vilaro T, Colin C, Bartout JD (2011) As-fabricated and heat-treated microstructures of the Ti–6Al–4V alloy processed by selective laser melting. Metall Mater Trans 42(10):3190–3199. https://doi.org/10.1007/s11661-011-0731-y

Wang P, Tan X, Nai MLS, Tor SB, Wei J (2016) Spatial and geometrical-based characterization of microstructure and microhardness for an electron beam melted Ti–6Al–4V component. Mater Des 95:287–295. https://doi.org/10.1016/j.matdes.2016.01.093

Wauthle R, Vrancken B, Beynaerts B, Jorissen K, Schrooten J, Kruth J-P, Van Humbeeck J (2015) Effects of build orientation and heat treatment on the microstructure and mechanical properties of selective laser melted Ti6Al4V lattice structures. Addit Manuf 5:77–84. https://doi.org/10.1016/j.addma.2014.12.008

Wegener K, Starr TL, Spierings AB (2013) Fatigue performance of additive manufactured metallic parts. Rapid Prototyp J 19(2):88–94. https://doi.org/10.1108/13552541311302932

Weingarten C, Buchbinder D, Pirch N, Meiners W, Wissenbach K, Poprawe R (2015) Formation and reduction of hydrogen porosity during Selective Laser Melting of AlSi10Mg. J Mater Process Technol 221:112–120. https://doi.org/10.1016/j.jmatprotec.2015.02.013

Witkin DB, Patel DN, Helvajian H, Steffeney L, Diaz A (2019) Surface treatment of powder-bed fusion additive manufactured metals for improved fatigue life. J Mater Eng Perform 28(2):681–692. https://doi.org/10.1007/s11665-018-3732-9

Wu J-H, Lin C-K (2002) Tensile and fatigue properties of 17–4 PH stainless steel at high temperatures. Metall Mater Trans 33(6):1715–1724. https://doi.org/10.1007/s11661-002-0180-8

Wu GQ, Shi CL, Sha W, Sha AX, Jiang HR (2013) Effect of microstructure on the fatigue properties of Ti–6Al–4V titanium alloys. Mater Des 46:668–674. https://doi.org/10.1016/j.matdes.2012.10.059

Wu AS, Brown DW, Kumar M, Gallegos GF, King WE (2014) An experimental investigation into additive manufacturing-induced residual stresses in 316L stainless steel. Metall Mater Trans A 45(13):6260–6270. https://doi.org/10.1007/s11661-014-2549-x

Wycisk E, Siddique S, Herzog D, Walther F, Emmelmann C (2015) Fatigue performance of laser additive manufactured Ti–6Al–4V in very high cycle fatigue regime up to 109 cycles. Front Mater. https://doi.org/10.3389/fmats.2015.00072

Wycisk E, Solbach A, Siddique S, Herzog D, Walther F, Emmelmann C (2014) Effects of defects in laser additive manufactured Ti–6Al–4V on fatigue properties. In Schmidt M, Vollertsen F, Merklein M (eds) 8th International Conference on Laser Assisted Net Shape Engineering (vol 56, pp 371–378). Elsevier. https://doi.org/10.1016/j.phpro.2014.08.120

Xu W, Sun S, Elambasseril J, Liu Q, Brandt M, Qian M (2015) Ti–6Al–4V additively manufactured by selective laser melting with superior mechanical properties. Jom 67(3):668–673. https://doi.org/10.1007/s11837-015-1297-8

Yadollahi A, Shamsaei N (2017) Additive manufacturing of fatigue resistant materials: challenges and opportunities. Int J Fatigue 98:14–31. https://doi.org/10.1016/j.ijfatigue.2017.01.001

Yadollahi A, Shamsaei N, Thompson SM, Elwany A, Bian L (2017) Effects of building orientation and heat treatment on fatigue behavior of selective laser melted 17–4 PH stainless steel. Int J Fatigue 94:218–235. https://doi.org/10.1016/j.ijfatigue.2016.03.014

Yadroitsev I, Bertrand P, Smurov I (2007) Parametric analysis of the selective laser melting process. Appl Surf Sci 253(19):8064–8069. https://doi.org/10.1016/j.apsusc.2007.02.088

Yang J, Yu H, Wang Z, Zeng X (2017) Effect of crystallographic orientation on mechanical anisotropy of selective laser melted Ti–6Al–4V alloy. Mater Charact 127:137–145. https://doi.org/10.1016/j.matchar.2017.01.014

Yang KV, Rometsch P, Jarvis T, Rao J, Cao S, Davies C, Wu X (2018) Porosity formation mechanisms and fatigue response in Al-Si-Mg alloys made by selective laser melting. Mater Sci Eng 712:166–174. https://doi.org/10.1016/j.msea.2017.11.078

Yasa E, Kruth JP (2011) Microstructural investigation of selective laser melting 316L stainless steel parts exposed to laser re-melting. Procedia Eng 19:389–395. https://doi.org/10.1016/j.proeng.2011.11.130

Zhai Y, Galarraga H, Lados DA (2015) Microstructure evolution, tensile properties, and fatigue damage mechanisms in Ti–6Al–4V alloys fabricated by two additive manufacturing techniques. In: Icsi 2015 the 1st International Conference on Structural Integrity Funchal, vol 114, pp 658–666. https://doi.org/10.1016/j.proeng.2015.08.007

Zhang S (2013) Cracking behavior and formation mechanism of TC4 alloy formed by selective laser melting. Ji Xie Gong Cheng Xue Bao 49(23):21. https://doi.org/10.3901/JME.2013.23.021

Zhang B, Li Y, Bai Q (2017) Defect formation mechanisms in selective laser melting: a review. Chin J Mech Eng 30(3):515–527. https://doi.org/10.1007/s10033-017-0121-5

Zhang D, Sun S, Qiu D, Gibson MA, Dargusch MS, Brandt M, Qian M, Easton M (2018a) Metal alloys for fusion-based additive manufacturing. Adv Eng Mater 20(5):1700952. https://doi.org/10.1002/adem.201700952

Zhang M, Sun CN, Zhang X, Goh PC, Wei J, Li H, Hardacre D (2018b) Effect of heat treatment on fatigue crack initiation of laser powder bed fusion stainless steel 316L. MATEC Web Conf 165:22006. https://doi.org/10.1051/matecconf/201816522006

Zhang M, Sun CN, Zhang X, Goh PC, Wei J, Li H, Hardacre D (2018c) Elucidating the relations between monotonic and fatigue properties of laser powder bed fusion stainless steel 316L. Jom 70(3):390–395. https://doi.org/10.1007/s11837-017-2640-z

Zhao X, Lin X, Chen J, Xue L, Huang W (2009) The effect of hot isostatic pressing on crack healing, microstructure, mechanical properties of Rene88DT superalloy prepared by laser solid forming. Mater Sci Eng A 504(1):129–134. https://doi.org/10.1016/j.msea.2008.12.024

Zhao X, Li S, Zhang M, Liu Y, Sercombe TB, Wang S, Hao Y, Yang R, Murr LE (2016) Comparison of the microstructures and mechanical properties of Ti–6Al–4V fabricated by selective laser melting and electron beam melting. Mater Des 95:21–31. https://doi.org/10.1016/j.matdes.2015.12.135

Zhao J, Easton M, Qian M, Leary M, Brandt M (2018) Effect of building direction on porosity and fatigue life of selective laser melted AlSi12Mg alloy. Mater Sci Eng A 729:76–85. https://doi.org/10.1016/j.msea.2018.05.040

Zheng B, Zhou Y, Smugeresky JE, Schoenung JM, Lavernia EJ (2008) Thermal behavior and microstructure evolution during laser deposition with laser-engineered net shaping: part II. Experimental investigation and discussion. Metall Mater Trans 39(9):2237–2245. https://doi.org/10.1007/s11661-008-9566-6